

**STRUCTURAL, OPTICAL, DIELECTRIC
AND MAGNETO-DIELECTRIC STUDIES
ON Fe DOPED LaGaO₃**

M.Sc. Thesis

By

PREETAM SINGH



**DISCIPLINE OF PHYSICS
INDIAN INSTITUTE OF TECHNOLOGY INDORE
JUNE, 2016**

STRUCTURAL, OPTICAL, DIELECTRIC AND MAGNETO-DIELECTRIC STUDIES ON Fe DOPED LaGaO₃

A THESIS

*Submitted in partial fulfillment of the
requirements for the award of the degree*

of
Master of Science

By

PREETAM SINGH



**DISCIPLINE OF PHYSICS
INDIAN INSTITUTE OF TECHNOLOGY INDORE
JUNE, 2016**



INDIAN INSTITUTE OF TECHNOLOGY INDORE

CANDIDATE'S DECLARATION

I hereby certify that the work which is being presented in the thesis entitled **“STRUCTURAL, OPTICAL, DIELECTRIC AND MAGNETO-DIELECTRIC STUDIES ON Fe DOPED LaGaO₃”** in the partial fulfillment of the requirements for the award of the degree of **MASTER OF SCIENCE** and submitted in the **DISCIPLINE OF PHYSICS, Indian Institute of Technology Indore**, is an authentic record of my own work carried out during the time period from July 2015 to June 2016 under the supervision of Dr. Pankaj R. Sagdeo and Dr. Rajesh Kumar, Associate Professors, Department of Physics, IIT Indore.

The matter presented in this thesis has not been submitted by me for the award of any other degree of this or any other institute.

**Signature of the student with date
(Preetam Singh)**

This is to certify that the above statement made by the candidate is correct to the best of my/our knowledge.

Signature of the Supervisor of

M.Sc. thesis #1 (with date)

(Dr. Pankaj R. Sagdeo)

Signature of the Supervisor of

M.Sc. thesis#2 (with date)

(Dr. Rajesh Kumar)

Preetam Singh has successfully given his M.Sc. Oral Examination held on **27th June, 2016.**

Signature(s) of Supervisor(s) of MSc thesis

Date:

Convener, DPGC

Date:

Signature of PSPC Member #1

Date:

Signature of PSPC Member #2

Date:

ACKNOWLEDGEMENTS

It is my pleasure to present this report with a sincere gratitude to all those people who have given me guidance, support and encouragement.

I have no words to express my feelings and gratitude to my parents for their love, care and support to complete my work. I also express my warm sense of thanks to all my friends.

First of all, I am thankful to Prof. Pradeep Mathur, Director, Indian Institute of Technology, Indore. This thesis would not have been possible without the help, support and patience of my guides Dr. Pankaj R. Sagdeo and Dr. Rajesh Kumar, Associate Professors, Department of Physics, IIT Indore. They have helped and encouraged me during this thesis work and always tried to overcome my doubts. I am grateful to my PSPC members Dr. Preeti A. Bhobe, Associate Professor, Department of Physics, IIT Indore and Dr. Sanjay Kumar Singh, Assistant Professor Department of Chemistry, IIT Indore for their valuable suggestions and guidance. I am thankful to all my lab mates Mr. Harimohan Rai, Mr. Shailendra K. Saxena, Mr. Vikash Mishra, Mrs. Priyanka Yogi, Md. Kamal Warshi, Mr. Suryakant Mishra, Miss. Pooja Yadav and Mr. Haardik Pandey for their kind help during my thesis work. I am heartily thankful to Mr. Harimohan Rai for his kind support during this work.

I would like to thank Dr. Archana Sagdeo, Dr. A. K. Sinha and Dr. Parasmani Rajput, Scientific Officers, RRCAT Indore for providing experimental facilities at RRCAT, Indore. I am grateful to all my classmates for their kind help and moral support. I am also thankful to all the faculty members at IIT Indore for their guidance and motivation and SIC IIT Indore is acknowledged for providing basic infrastructure facilities.

Preetam Singh

Dedicated
To
My Parents

Abstract

Multifunctional materials are of very high research interest due to their potential applications and interesting physics. LaGaO_3 (LGO) has been established as a prototype fuel cell material having perovskite structure. It is also a good substrate material for the growth of superconducting thin films. LGO exhibits room temperature (RT) orthorhombic crystal symmetry with *pnma* space group and it undergoes through various structural phase transformations under different temperature and pressure conditions. Moreover, this perovskite exhibits different interesting properties with the doping of Mn ions. However, transition metal (TM) ion doped LGO compound may have different potential scopes which have not been explored so far. For example - it may have the potential to be a good candidate for optoelectronic devices and it may also display magneto-dielectric (MD) properties near room temperature as it exhibits- (i) temperature (almost up to 400K) and frequency independent dielectric properties (dielectric permittivity ϵ' and $\tan\delta$) and (ii) structural phase transition well above the room temperature (418 K). Keeping this all in view, in present work, a series of Fe doped LGO samples i.e., $\text{LaGa}_{1-x}\text{Fe}_x\text{O}_3$ (LGFO); $0 \leq x \leq 1$ is prepared by solid-state reaction route. The purity of structural phase of all prepared polycrystalline LGFO samples has been validated (considering orthorhombic symmetry with *pnma* space group) through x-ray diffraction (XRD) experiments by refining the XRD data with the help of Fullprof Rietveld refinement package. Vegard's law has been verified for the present LGFO series and corresponding 'bowing' parameter has been calculated by using refined lattice parameters and the band gap of LGFO samples respectively. The band gap for all presently studied samples is determined through diffuse reflectance spectroscopy (DRS) based on the formalism of Kubelka-Munk function and Tauc's relation. LGFO sample with $x=0.3$ exhibits a noticeable MD effect (i.e. change in the value of dielectric constant due to the application of magnetic field). The trends of changes observed in dielectric constant (ϵ') and $\tan\delta$ due to the application of magnetic field suggest that the observed MD effect should be an intrinsic property of these samples. In order to estimate the intrinsic and resistive contributions of observed RT MD

effect, dc MR (using four probe geometry) and frequency dependent magneto resistance measurements by means of impedance spectroscopy (MRIS) along with the iodometric titration and XANES measurements has been carried out at RT. Present MRIS analysis suggests that at frequencies corresponding to grain contribution ($\geq 10^6$ Hz for present samples), the observed MD phenomenon appears to be an intrinsic property of presently studied samples whereas at lower probing frequencies ($< 10^6$ Hz) the observed change appears to be MR (considering frequency dependent resistance) dominated possibly due the coexistence Fe^{3+} and Fe^{4+} . The coexistence of Fe^{3+} and Fe^{4+} in $\text{LaGa}_{0.7}\text{Fe}_{0.3}\text{O}_3$ has been validated through iodometric titration and Fe K-edge XANES measurements. Present study reveals the possibility of RTMD coupling in LGFO (x=0.3).

Key Words: Structural analysis; Optical band-gap; Dielectric and magneto-dielectric properties.

LIST OF PUBLICATIONS

1. P.R. Sagdeo*, Preetam Singh, Hari Mohan Rai, Rajesh Kumar, Archana Sagdeo, and Parasmani Rajput, “*Vegard’s law, optical band gap and bowing parameter of Fe doped LaGaO₃*”(arxiv : 1603.04961).
2. Hari Mohan Rai^{a)}, PreetamSingh^{a)}, Shailendra K. Saxena, Vikash Mishra, Rajesh Kumar, Archana Sagdeo and P.R. Sagdeo* “*Observation of Magneto-Dielectric effect in LaGa_{0.7}Fe_{0.3}O₃*” (under review: RSC Advances).

CONTENTS

Contents		Page No.
Chapter 1:	Introduction and Origin of the Problem	01
1.1	Magnetoelectrics and Multiferroicity	03
1.2	Structure of LaGaO ₃	05
Chapter 2:	Experimental Techniques	07
2.1	Sample Preparation Process	07
2.2	Characterization Techniques	09
(a)	X- Ray Diffraction (XRD)	09
(b)	Diffuse Reflectance Spectroscopy (DRS)	12
(c)	Impedance Spectroscopy (IS)	14
(d)	Titration	17
(e)	XANES (X-Ray Absorption Near Edge Spectroscopy)	19
Chapter 3:	Results and Discussions	23
3.1	Structural Studies (XRD)	23
3.2	Optical Properties Analysis	27
3.3	Dielectric and Magneto-dielectric Properties	33
Chapter 4:	Summary, Conclusion and Future Scope	49
References	List of References	51

LIST OF FIGURES

Figure No.	Caption	Page No.
1.1	Variation of dielectric constant of LGO with temperature.	02
1.2	Schematic diagram of multiferroics and magneto-dielectrics	04
1.3	Perovskite Structure of LaGaO ₃	06
2.1	Diffraction of X-ray by a crystal	09
2.2	Schematic diagram of X-ray diffractometer	10
2.3	Production of K _α and K _β lines	11
2.4	Schematic Diagram of Light Scattering from a powdered sample	12
2.5	Experimental set up for diffuse reflectance measurement (a) Carry 60 UV-Vis spectrometer, (b) an integrating sphere attachment to detect diffuse reflectance	14
2.6	Schematic diagram of series LCR ac bridge	15
2.7	(a) Phase Diagram of voltage and current and (b) phase diagram of impedance of an LCR Circuit	16
2.8	(a) LCR Meter and (b) Constant current source, Digital Gauss meter and magnet	16
2.9	Titration : Sequential step wise change in color upto end points	19
2.10	X-ray absorption spectrum with XANES region	20
2.11	The oxidation states of Mn references (i.e., 0, 2+, 3+ and 4+) as a function of the corresponding K-edge energies. The red curve is displaying a 2 nd order	20

	polynomial fit of this data	
3.1.1	Lab Source Room Temperature(RT) XRD Data of all Prepared Samples	23
3.1.2	Rietveld refined powder x-ray diffraction data for $\text{LaGa}_{0.7}\text{Fe}_{0.3}\text{O}_3$. The insets (a) and (b) show the magnified views for (121) at $2\theta = 32.45$ and (442) at $2\theta = 95.44$ respectively	24
3.1.3	(a) Lab source XRD data of $\text{LaGa}_{1-x}\text{Fe}_x\text{O}_3$ ($x=0.2, 0.4, 0.6, 0.8, 1.0$) and the the magnified view of (121) plane is shown in inset (b)	25
3.1.4	Variation of lattice parameters as a function of Fe doping	27
3.2.1	The equivalent Tauc plot for indirect band-gap of $\text{LaGa}_{1-x}\text{Fe}_x\text{O}_3$ samples	29
3.2.2	The equivalent Tauc plot for direct band-gap of $\text{LaGa}_{1-x}\text{Fe}_x\text{O}_3$ samples	29
3.2.3	(a) Intrinsic band-diagram of solids and (b) Band-diagram of solids due to orbital overlapping	32
3.2.4	(a) Fitting of band- gap for Bowing parameter calculation using direct band gap and (b) Fitting of band-gap for Bowing parameter calculation using indirect band gap	32
3.3.1	The behavior of dielectric constant (a) and dielectric loss of $\text{LaGa}_{1-x}\text{Fe}_x\text{O}_3$ (for some value of x) as a function of frequency and Fe composition	33
3.3.2	(a) Cole-cole diagram of Fe- doped LaGaO_3 for whole probing frequency and (b) the enlarged version of cole-cole diagram at higher frequency	35
3.3.3	Change in dielectric constant of $\text{LaGa}_{1-x}\text{Fe}_x\text{O}_3$	36

	(x=0.02,0.25,0.30,0.40) with the application of magnetic field (H=1T)	
3.3.4	Room-temperature (a) dielectric constant (ϵ') and (b) dielectric loss ($\tan\delta$) as a function of frequency measured in the absence (H=0.0 T) and presence (0.8 T) of magnetic field for LaGa _{0.7} Fe _{0.3} O ₃ . In (a), insets show magnified view of data at corresponding frequency ranges. In (b) the data corresponding to entire range of probing frequencies is shown in the inset (i) and high frequency data is magnified as main panel for clarity. The inset (ii) displays magnified view of first broad peak	37
3.3.5	Room-temperature loss tangent ($\tan\delta$) as a function of frequency measured in the absence (H= 0.0T) and presence (0.8T) of magnetic field. The data is shown only for higher frequencies to demonstrate that the value of $\tan\delta$ increases with increasing magnetic field even at the frequencies of > 1 MHz and its value remains < 1 even at such high frequencies	40
3.3.6	The trends of Room-temperature (RT) -(a) Magneto-capacitance (MC%) and (b) Magneto-loss (ML%) as a function of applied magnetic fields for LaGa _{0.7} Fe _{0.3} O ₃ measured at selected frequencies from 100 Hz to 10 MHz. Both MC% and ML% are increasing with magnetic field for probing frequency of $\geq 10^6$ Hz. On the other hand at frequencies $< 10^6$ Hz MC% and ML% are changing oppositely due to increasing magnetic field. Both MC% and ML% have been calculated by using the formulae shown in corresponding figures. Where, $\epsilon'(0)$	41

	and $\epsilon'(H)$ are the dielectric constant correspondingly in the absence ($H=0.0$ T) and presence of magnetic field ($H=0.8$ T) whereas $\tan\delta(0)$ and $\tan\delta(H)$ represent loss tangent respectively in the absence ($H=0.0$ T) and presence of magnetic field ($H=0.8$ T)	
3.3.7	Room-temperature MC% as a function of probing frequency for different magnetic fields. Inset displays MC% data at higher frequencies ($\geq 10^6$ Hz) to show that the observed MD effect is significant even at such high frequencies also. MC% has been calculated by using the formula shown in figure. Where, $\epsilon'(0)$ and $\epsilon'(H)$ are the dielectric constant correspondingly in the absence ($H=0.0$ T) and presence of magnetic field ($H= 0.8$ T)	42
3.3.8	Room temperature I-V plot drawn by measuring the voltage for different values of current in the absence ($H=0.0$ T) and presence ($H=0.7$ T) of magnetic field by using standard four-probe method	44
3.3.9	Room-temperature Cole-Cole diagram of $\text{LaGa}_{0.7}\text{Fe}_{0.3}\text{O}_3$ plotted for frequencies ranging between 20 Hz to 10 MHz. is shown in inset (b) and only high frequency data (enclosed by a rectangular green box in (b) is magnified as main panel in (a). The data is measured in the absence ($H=0$ T) and presence of magnetic field (0.8 T)	45
3.3.10	Representative XANES spectra for the prepared Fe doped LaGaO_3 samples	47

LIST OF TABLES

Table No.	Caption	Page No.
3.1.1	Values of lattice constants with Fe-doping	26
3.2.1	Indirect Band-gaps with Fe-Composition. Here E_{g1} and E_{g2} are corresponding to two different absorption edges	30
3.2.2	Direct Band-gaps with Fe-Composition. Here E_{g1} and E_{g2} are corresponding to two different absorption edges	31
3.3.1	Change observed in the value of room temperature ϵ' (in %) due to the application of magnetic fields of 0.2 T and 0.8 T	39
3.3.2	The frequencies (Hz) corresponding to maximum value observed in broad peak of MC% for the magnetic fields of 0.2 T and 0.8 T	43

Acronyms

LGO	LaGaO ₃
RT	Room Temperature
TM	Transition Metal
MD	Magneto-Dielectric
LGFO	LaGa _{1-x} Fe _x O ₃
XRD	X-Ray Diffraction
DRS	Diffuse Reflectance Spectroscopy
MR	Magneto Resistance
MRIS	Magneto Resistance Impedance Spectroscopy
XANES	X-Ray Near Edge Spectroscopy
RTMD	Room Temperature Magneto-Dielectric
ME	Magneto-Electric
IS	Impedance Spectroscopy
LR	Inductance and Resistance
CR	Capacitance and Resistance
FDMR	Frequency Dependent Magneto Resistance

CHAPTER 1

Introduction and Origin of the Problem

The search for the new materials for various electronics applications have dominated the research worldwide particularly after the development of silicon based tiny transistors/integrated circuits and BaTiO₃ based tiny capacitors. During last four decades the nature of electronic devices has witnessed huge changes. The discovery of the spin valve and the signals transmission using optical cables are the real examples[1,2]. The conceptual developments in the field of electronics, photonics and spintronics are now leading to the discovery of new type of devices and materials these materials falls in to the category of highly correlated electron system. In highly correlated electron system the charge, spin and lattice degree of freedoms and interactions between them critically controls the various properties of a given material[3]. Thus by application of external magnetic field it is now possible to control the ferroelectric polarization[4,5]. The mutual control on the electric and magnetic polarization is now attracting attention of scientific community due to their possible applications as novel spin based devices[4] and also to enhance the memory density in data storage devices[6].

Presently the candidate materials in this category are limited and show the magneto-dielectric response either at very high value of magnetic field or at low temperatures which limits the practical application of such devices. But interestingly it pointed out that the value of such magneto-dielectric response is highest very close to transition temperature[7].

Recently we have demonstrated the magneto-dielectric effect at room temperature in Mn doped LaGaO₃[8]. It should be noted that LaGaO₃ known to show the structural phase transition at 418K and with doping this structural phase transition temperature decreases and

approaches very close to room temperature[9,10]. Thus doping of magnetic cation at Gallium site may lead decrease in the structural phase transition temperature and may also lead to the magnetic interaction. Further it should be noted that LaGaO₃ is well known materials for solid state fuel cells[11,12]. As the band gap of the LaGaO₃ is very close to 4.0 eV[13,14] so this material has been vastly explored for optoelectronic applications due to its excellent photo luminescence properties[15–17] and recently Mn doped LaGaO₃ is proposed as new room temperature magneto-dielectric material[8] with high value of dielectric constant[18]. Further the theoretical report on static dielectric constant of lanthanide gallates[19] suggest that the dielectric constant of LaGaO₃ (LGO) is largest out of all studied lanthanide gallates, the result of A. Senyshyn et al. are represented in fig.(1.1). Dube et al. have reported temperature dependent behavior of dielectric properties for LaGaO₃, it is observed that the value of ϵ' and dielectric loss ($\tan\delta$) is almost independent of temperature and frequency up to ~400 K with very low value of dielectric

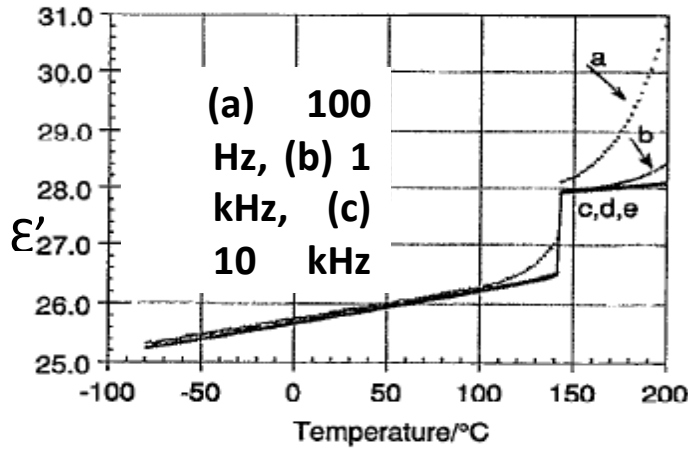


Fig.(1.1): Variation of dielectric constant of LGO with temperature.

loss of $\sim 1 \times 10^{-4}$ [20–23]. Thus the LaGaO₃ appears to be the potential material for various electronic applications[1,12,18]. Keeping the above in view, here we aim to study the effect of Fe doping on the structural,

optical, dielectric and magneto-dielectric properties of $\text{LaGa}_{1-x}\text{Fe}_x\text{O}_3$ ($0 \leq x \leq 1$). At this juncture it is important to note that LaFeO_3 known to show the multiferroic properties[21] further the end compound LaGaO_3 and LaFeO_3 and solid solution i.e. intermediate compound possesses orthorhombic symmetry with $Pnma$ [8,24,25] space group. Thus the Fe doping in LaGaO_3 expected to create minimum structural disorder and may be ideal candidate to study the effect of Fe doping on the dielectric and optical properties. Further due to difference in the ionic radius of Ga^{+3} and Fe^{+3} it is expected that with Fe doping in LaGaO_3 may lead to systematic variation in lattice parameters as observed in similar perovskite oxides[24] and consequently variation in band gap[24,25].

In the following section we have briefly discussed the important concepts related to the present work.

1.1 Magneto-electrics and Multiferroicity:

The field of research that we are dealing with has a complicated classification and typically involves terms such as ‘multiferroic’ and ‘magneto-dielectric’ whose overlap is shown in fig.(1.2). By the original definition, a single-phase multiferroic material is one that possesses two or all three of the so-called ‘ferroic’ properties/orders simultaneously i.e. ferroelectricity, ferromagnetism and ferroelectricity whereas magneto-electric (ME) coupling may exist whatever the nature of magnetic and electrical order parameters, Hall effect observed in most of the non-magnetic semiconductors (such as Si and Ge etc.) may be best example of magneto-electric effect[26]. Magneto-electric coupling may arise directly due to the coupling between the two or more force fields (local electric, magnetic or strain field) present intrinsically in sample or due to coupling between internal force field and external perturbations. At times, strain-mediated indirect magneto-electric coupling found to enhance the magneto-electric coupling.

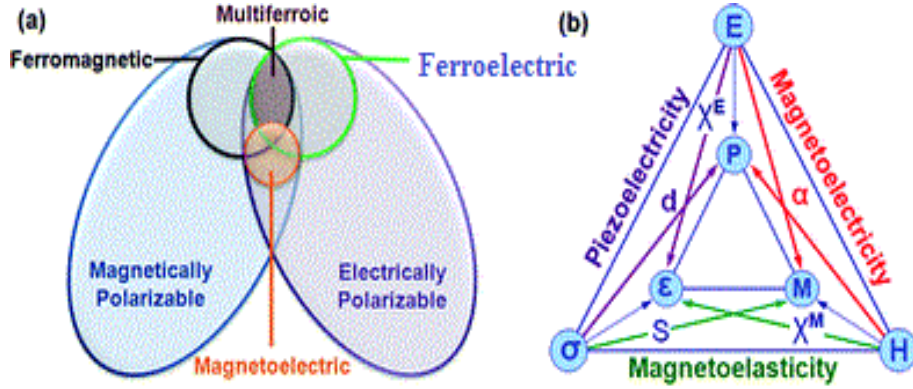


Fig.(1.2): Schematic diagram of multiferroics and magneto-dielectrics[26].

Naturally, magnetic field is coupled with electric field as shown below by the Maxwell's equations. Equations (i) and (ii) show the relation between electric and magnetic field in free space and this relation is also given by equation (iii) which shows that a small coupling between B and E but in materials magnetic permeability (μ_r) and electric permittivity (ϵ_r) will be different from free space and hence electromagnetic coupling may enhance, as we can see from following maxwell's equations.

$$\nabla \times E = -\frac{dB}{dt} \dots (i)$$

$$\nabla \times B = \mu J + \epsilon \mu \frac{dE}{dt} \dots (ii)$$

$$B = cE \dots (iii),$$

Where B and E are magnetic and electric fields respectively and $c = \frac{1}{\sqrt{\mu_o \epsilon_o}}$ $\sim 10^8$ and μ_o and ϵ_o are the permeability and permittivity of free space respectively.

$$\nabla \times E = -\frac{dB}{dt} \dots (iii)$$

$\nabla \times B = \mu J + \epsilon \mu \frac{dE}{dt} \dots (iv)$, where J is the current density vector, $\mu = \mu_o \mu_r$ and $\epsilon = \epsilon_o \epsilon_r$ and μ_r and ϵ_r are the relative permeability and permittivity of medium respectively.

Alternatively, magneto-electric effect in a crystal is traditionally described in Landau theory by writing the free energy F of the system in terms of an applied magnetic field H and an applied electric field. Using Einstein summation convention F can be written as[27]:

$$-F(E, H) = 1/2 \epsilon_0 \epsilon_{ij} E_i E_j + 1/2 \mu_0 \mu_{ij} H_i H_j + \alpha_{ij} E_i H_j + \beta_{ijk} /2 E_i H_j H_k + \gamma_{ijk} /2 H_i E_j E_k + \dots (1.1)$$

The first term on the right hand side describes the contribution resulting from the electrical response to an electric field, where $\epsilon_{ij}(T)$ is relative permittivity. The second term is the magnetic equivalent of the first term, where $\mu_{ij}(T)$ is relative permeability. The third term describes linear magneto-electric coupling via $\alpha_{ij}(T)$. Other terms represent higher-order magneto-electric coupling coefficients. The magneto-electric effect can be established in the form $P_i H_j$ or $M_i E_j$ by differentiating F . One obtains

$$(H_j) = \alpha_{ij} H_j + \beta_{ijk} /2 H_j H_k + \dots (1.2)$$

$$(E_j) = \alpha_{ij} E_i + \gamma_{ijk} /2 E_j E_k + \dots (1.3)$$

Term α_{ij} is designated as the linear magneto-electric effect and corresponds to the induction of polarization by a magnetic field or a magnetization by an electric field. Materials exhibiting ME effect are Cr_2O_3 , $BiMnO_3$, $BiFeO_3$. Unfortunately, the magneto-electric effect is usually too small to be practically applicable as term α_{ij} is limited by the relation:

$$\alpha_{ij}^2 \leq \epsilon_0 \mu_0 \epsilon_{ii} \mu_{jj} \dots (1.4)$$

Keeping above view in mind we have decided to work with materials in which we are expecting the above properties.

1.2 Structure of LaGaO₃:

Lanthanum Gallate(LaGaO₃) possesses ABO₃ type perovskite structure[28] as shown in fig.(1.3), here A and B are cations and O is an anion or ligand. For cubic systems these anions are present at the centre of each faces and all of them are equidistant from the central atom (B-cation) which forms a centrosymmetric octahedron around B-cation. Due to this

fact no net dipole moment found in this material. But once their symmetry is broken a net dipole moment arises and hence ferroelectricity can be induced in the material. The doping with transition metal element such as Fe, Ni, Mn etc. at B site may lead to magnetic interaction in the prepared sample.

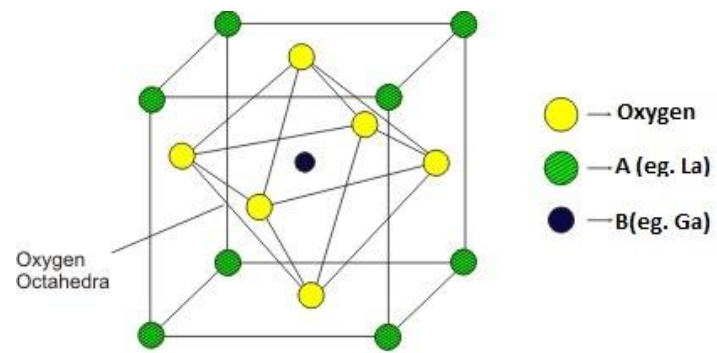


Fig.(1.3): Perovskite Structure of LaGaO_3 .

CHAPTER 2

Experimental Techniques

In this chapter some of the experimental techniques useful for the present project work are discussed. The work carried in this project mainly deals with the following experimental techniques.

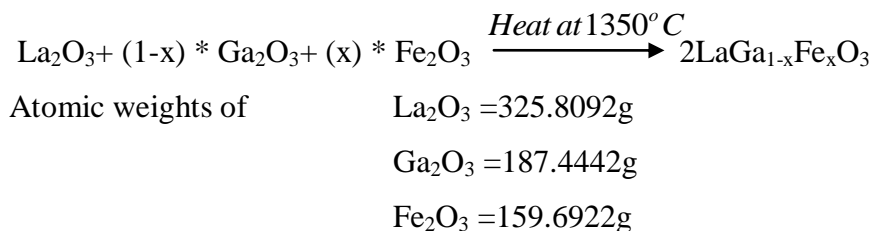
2.1 Sample Preparation Process

2.2 Characterization Techniques

- (a) X- Ray Diffraction (XRD)
- (b) Diffuse Reflectance Spectroscopy (DRS)
- (c) Impedance Spectroscopy (IS)
- (d) Titration
- (e) XANES (X-Ray Absorption Near Edge Spectroscopy)

2.1 Sample Preparation Process:

We have prepared Fe-doped LaGaO₃ i.e. LaGa_{1-x}Fe_xO₃ by conventional solid state reaction method[8] by mixing the constituents powder oxides in their proper stoichiometry of which calculation is given below. Solid-state reaction route is the most common technique for the preparation of polycrystalline samples. In this method, very fine powders are used as starting materials. These solid powders usually do not react at room temperature over normal time scales and hence it becomes necessary to heat these powders at much higher temperatures (800°C to 1600°C). The reaction may be written in the following form.



$$\text{LaGa}_{1-x}\text{Fe}_x\text{O}_3 = 138.9055 + 69.723*(1-x) + 55.847*x + 47.9982$$

For example $x=0.1$, then weight of $\text{LaGa}_{0.9}\text{Fe}_{0.1}\text{O}_3 = 138.9055 + 69.723*0.9 + 55.847*0.1 + 47.9982 = 255.2391\text{g}$

Weight (gm) of La_2O_3 for 1 mole of $\text{LaGa}_{0.9}\text{Fe}_{0.1}\text{O}_3 = 325.8092/2 = 162.9046\text{g}$

Weight (gm) of Ga_2O_3 for 1 mole of $\text{LaGa}_{0.9}\text{Fe}_{0.1}\text{O}_3 = (187.4442/2)*0.9 = 84.3499\text{g}$

Weight (gm) of Fe_2O_3 for 1 mole of $\text{LaGa}_{0.9}\text{Fe}_{0.1}\text{O}_3 = (159.6922/2)*0.1 = 7.9846\text{g}$

Now the weight of La_2O_3 for 1 gm of $\text{LaGa}_{0.9}\text{Fe}_{0.1}\text{O}_3 = 162.9046/255.2391 = 0.63824\text{g}$

Similarly the weight of Ga_2O_3 for 1 gm of $\text{LaGa}_{0.9}\text{Fe}_{0.1}\text{O}_3 = 84.3499/255.2391 = 0.33047\text{g}$

And the weight of Fe_2O_3 for 1 gm of $\text{LaGa}_{0.9}\text{Fe}_{0.1}\text{O}_3 = 7.9846/255.2391 = 0.03128\text{g}$

After weighing these oxides we have used the following steps to prepare samples:

- a) Mix the oxides and grind it by using Agate mortar and pestle in Iso-Propyl Alcohol (IPA) for 4-5 hours.
- b) Then heat the sample in furnace at 1000°C for 24 hours with a controlled heating rate of 1° per minute.
- c) After 24 hours cool the sample up to 350°C with a cooling rate of 1° per minute, after that, cool the sample naturally up to room temperature after switching off the furnace.
- d) Repeat the steps (a) to (c) for second heating at 1250°C .
- e) After that the circular pellets of 1 mm thickness and about 13 mm diameter (by using almost half quantity of corresponding powder sample) were prepared by applying a high pressure by means of hydraulic pressure pelletizer.
- f) These prepared pellets and powdered samples have been sintered separately in air at 1300°C for 24 hours.

After preparing samples following experimental techniques are used to characterize the samples.

2.2 Characterization Techniques:

a). X-Ray Diffraction(XRD):

Principle: Max Von Laue, in 1912 discovered that the crystalline substances act like a three dimensional gratings for x-ray wavelengths similar to the spacing of planes in crystal lattice. X-ray study is now common technique for the study of crystal structure and atomic spacing. X-ray diffraction is based on constructive interference of monochromatic x-rays and a crystalline sample[29,30]. These X-rays are generated by a cathode ray tube, filtered to produce monochromatic radiation, collimated to concentrate, and directed toward the sample. The interaction of the

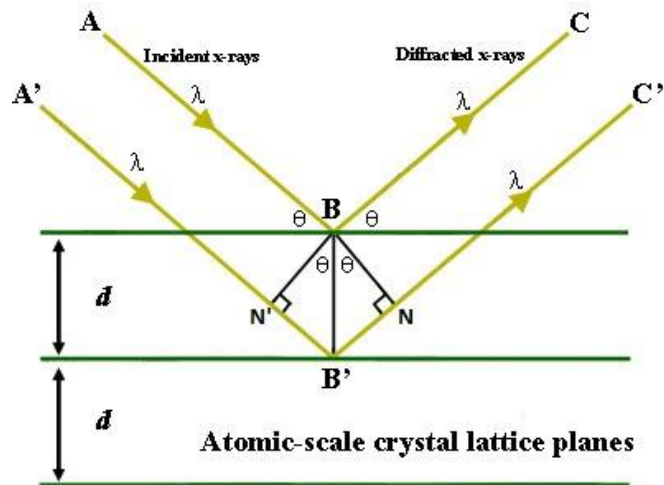


Fig.(2.1): Diffraction of X-ray by a crystal.

incident rays with the sample produce constructive interference when conditions satisfy Bragg's law ($2d \sin \theta = n\lambda$) as discussed below (Fig.2.1):

The path difference between C and C'

$$\begin{aligned}
 &= N'B' + B'N \\
 &= BB' \sin \theta + BB' \sin \theta
 \end{aligned}$$

So, path difference between C and C'

$$=2BB'\sin\theta =2d\sin(\theta)$$

For the constructive interference the path difference should be integer multiple of wavelength λ . So the Bragg's condition for constructive interference,

$$2d\sin\theta = n\lambda,$$

where n is an integer.

This law relates the wavelength of electromagnetic radiation to the diffraction angle and the lattice spacing in a crystalline sample. These diffracted X-rays are then detected, processed and counted. By scanning the sample through a range of 2θ angles, all possible diffraction directions of the lattice should be attained due to the random orientation of the powdered material. Conversion of the diffraction peaks to d-spacings allow identification of the minerals because each mineral has a set of unique d-spacings. Typically, this is achieved by comparison of d-spacings with standard reference patterns.

Instrumentation: X-ray diffractometer consists of three parts: an X-ray tube, sample holder and an X-ray detector as shown in fig.(2.2). The X-rays are produced in cathode ray tube by heating filament to produce electrons, accelerating the electrons towards the target by applying a field and bombarding the target material with electrons. When electrons have

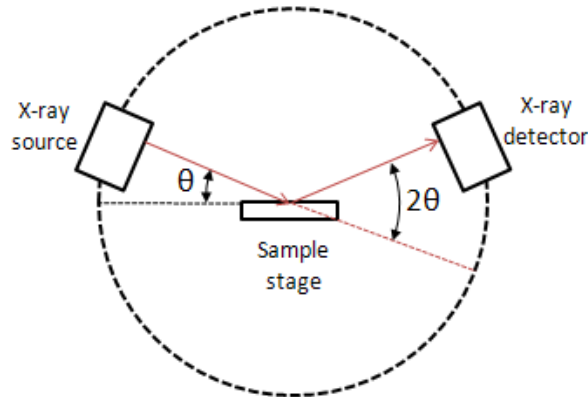


Fig.(2.2): Schematic diagram of X-ray diffractometer.

sufficient energy to dislodge inner shell electrons of the target material, characteristic spectra of X-rays are produced. The spectra consist of several components of rays, the most common are K_α and K_β line. K_α consists of $K_{\alpha 1}$ and $K_{\alpha 2}$ as shown in fig.(2.3). $K_{\alpha 1}$ has a slightly shorter wavelength and twice the intensity as $K_{\alpha 2}$. The specific wavelengths are characteristic of the target material (Cu, Fe, Mo, Cr). Filtering, by foils or crystal monochromators, is required to produce monochromatic X-rays needed for diffraction. $K_{\alpha 1}$ and $K_{\alpha 2}$ are sufficiently close in wavelength such that a weighted average of the two is used. Copper is the most common target material for single-crystal diffraction, with Cu- K_α radiation = 1.5418Å. These X-rays are collimated and directed onto the sample. As the sample and detector are rotated, the intensity of the reflected X-rays is recorded. When the geometry of the incident X-rays impinging the sample satisfies the Bragg Equation, constructive interference occurs and a peak in intensity occurs. These peak intensities are different for different planes as electron density varies in different planes. A detector records and processes this X-ray signal and converts the signal to a count rate which is

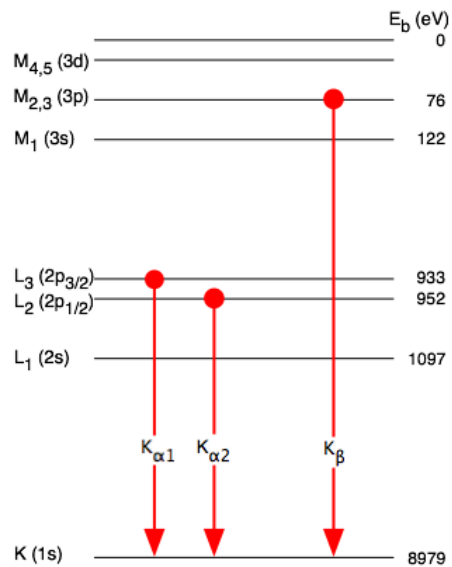


Fig.(2.3): Production of K_α and K_β lines.

then output to a device such as a printer or computer monitor.

b). Diffuse Reflectance Spectroscopy(DRS):

Principle: In DRS technique[31] diffuse reflectance (which is related to absorption of the sample through Kubelka-Munk equation) is detected. When light falls on the surface of a powdered sample, it is reflected in specular and non-specular directions; as shown in fig.(2.4). Some part of the light undergoes multiple scattering inside the sample and fraction of this part is emitted back into the detector. Due to the finite absorption coefficient of the sample, as the diffuse reflected light is reflected or passes through the powder, it becomes weaker i.e. loses its intensity and this loss of intensity is a function of absorption coefficient of sample which is function of λ of incident beam. This results in a diffuse reflected

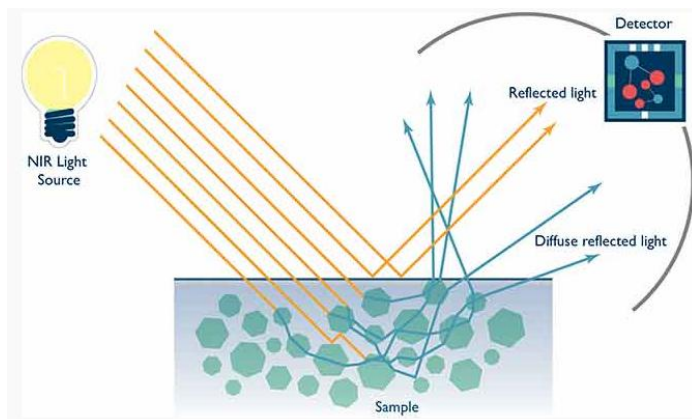


Fig.(2.4): Schematic Diagram of Light Scattering from a powdered sample.

spectrum, however, in regions (wavelength) where the powder exhibits strong absorption, one can see sharp/moderate jump in the observed DRS spectra. The DRS data may be quantitatively analyzed in the terms of Kubelka-Munk (K-M) function $f(R_{\infty})$ given by.

$$f(R_{\infty}) = \frac{(1 - R_{\infty})^2}{2R_{\infty}} \dots\dots\dots(2.1)$$

Where, R_{∞} is the absolute reflectance, K is the absorption coefficient, and S is the scattering coefficient. However, due to the difficulty in measuring the absolute reflectance R_{∞} , in practice, the comparative reflectance r_{∞} with respect to a standard powder such as BaSO_4 or white paper or KCl of which K is very small (near zero) in the actual measurement range.

$$R_{\infty} = \frac{r'_{\infty}}{r_{\infty}}$$

Where r_{∞}' is reflectance from sample and r_{∞} is reflectance from standard sample.

If the material scatters in a perfectly diffuse manner, the scattering function S is nearly constant with wavelength[18] and the Kubelka–Munk function can be related/proportional to the absorption coefficient (α) as

$$F(R_{\infty}) \propto \alpha \propto \frac{(h\nu - E_g)^{1/n}}{h\nu} \dots (2.2)$$

Here n has the value of 2 for direct band-gap transitions, while n is equal to 1/2 for an indirect band-gap transition. Thus, a plot between $[F(R_{\infty}) \times h\nu]^n$ versus $h\nu$ yields a straight line and the intercept on the energy axis gives the value of the band-gap.

Working: A diffuse reflectance has been measured by an attachment to an UV-Vis. spectrometer. Here an integrating sphere detector (fig. 3.4 b) is attached to Carry 60 (Agilent) UV-Visible instrument (fig. 3.4a). In Carry 60 white lamp sources (Xenon lamp) is used and grating is used to select monochromatic wavelength. Here in this set up the initial beam is splitted into two parts, one is taken as reference beam and second goes on the sample. Finally the output is compared to the reference beam and data has been collected. Since output photons comes through scattering from the samples so there is an integrating sphere detector.



Fig.(2.5): Experimental set up for diffuse reflectance measurement (a)Cary 60 UV-Vis spectrometer, (b) an integrating sphere attachment to detect diffuse reflectance.

c) Impedance Spectroscopy (IS): Impedance spectroscopy or dielectric spectroscopy measures the dielectric properties of a medium as a function of frequency. It is based on the interaction of external electric field with dipole moment of the medium, usually expressed by permittivity. Here we are using LCR meter for determining these properties.

Principle: LCR meter works on the principle of ac bridges, one schematic diagram of an ac bridge is shown in fig.(2.6). The working principle of circuit is shown below:

Applying Kirchoff's voltage law, we obtain

$$V(t) - V_R(t) - V_L(t) - V_C(t) = V(t) - IR - L \frac{dI}{dt} - \frac{Q}{C} = 0$$

$$\text{or, } IR + L \frac{dI}{dt} + \frac{Q}{C} = V_o \sin \omega t$$

Assuming that $I = \frac{dQ}{dt}$, then

$$L \frac{d^2Q}{dt^2} + R \frac{dQ}{dt} + \frac{Q}{C} = V_o \sin \omega t \dots(2.3)$$

Solution of above equation can be given as

$$Q(t) = Q_o \cos(\omega t - \delta)$$

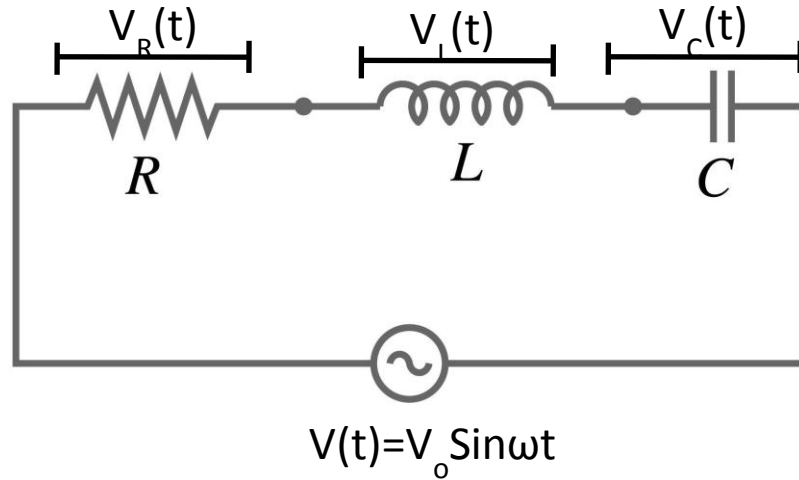


Fig. (2.6): Schematic diagram of series LCR ac bridge.

Where, amplitude and phase are respectively,

$$Q_o = \frac{V_o/L}{\sqrt{(R\omega/L)^2 + (\omega - 1/LC)^2}} = \frac{V_o}{\omega\sqrt{R^2 - (\omega L - \frac{1}{\omega C})^2}}$$

$$= \frac{V_o}{\omega\sqrt{R^2 - (X_L - X_C)^2}} \quad \dots(2.4)$$

And $\tan \delta = \frac{1}{R} \left(\omega L - \frac{1}{\omega C} \right) = \frac{X_L - X_C}{R} \dots(2.5)$

The corresponding current, $I_t = \frac{dQ}{dt} = I_o \sin(\omega t - \delta) \dots(2.6)$

With an amplitude $I_o = -Q_o \omega = -\frac{V_o}{\sqrt{R^2 + (X_L - X_C)^2}} \dots(2.7)$

Generally, the device under test is subject to an *ac* voltage source. The LCR meter measures the current through the device and also the phase difference between the current and voltage as shown in fig. (2.7 (a)) and also it measures the impedance i.e real and imaginary parts of resistance and phase difference ($\tan \delta$) as shown in fig.(2.7(b)). The Phase difference ($\tan \delta$) shows the dielectric loss. It also measures the equivalent capacitance, inductance etc. of the circuit. The meter must assume that

either one usually adopted, is that LR measurements have the elements in series (as would be encountered in an inductor coil) and that CR measurements have the elements in parallel (as would be encountered in measuring a capacitor with a leaky dielectric).

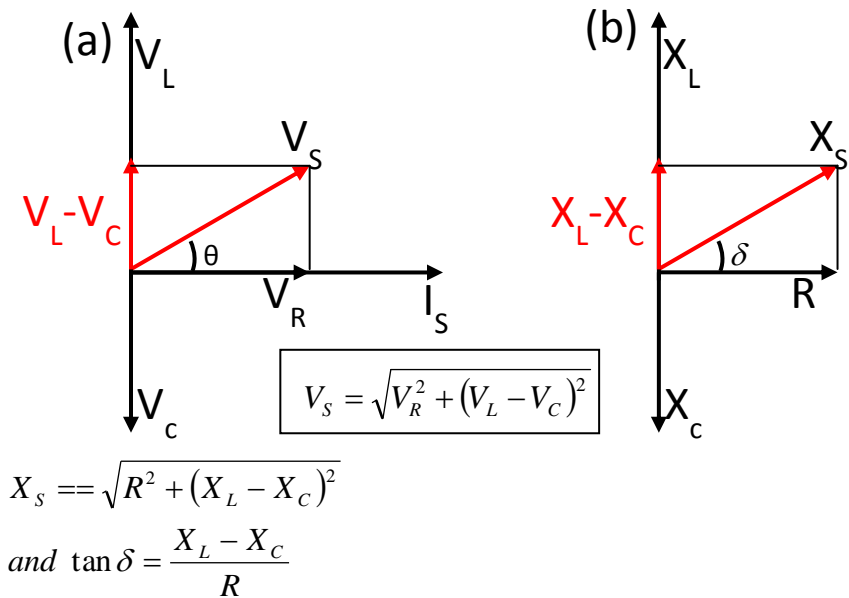


Fig.(2.7): (a) Phase diagram of voltage and current and (b) phase diagram of impedance of an LCR circuit.

Working: For the present studies we have used the samples in the form of pellet coated with silver on both the side. The short circuit and open circuit compensations were performed in order to get rid of contributions to the

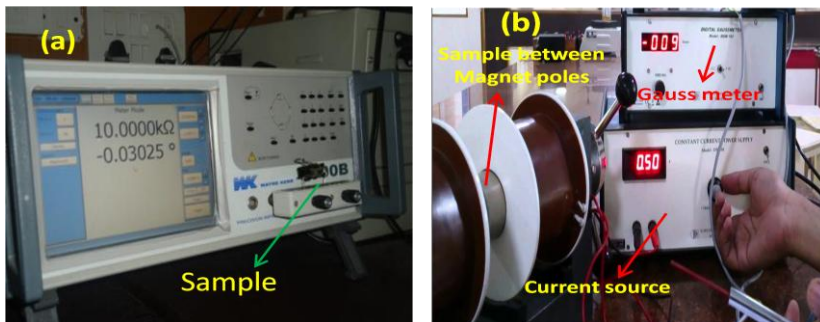


Fig.(2.8): (a) LCR Meter and (b) Constant current source, Digital Gauss meter and magnet.

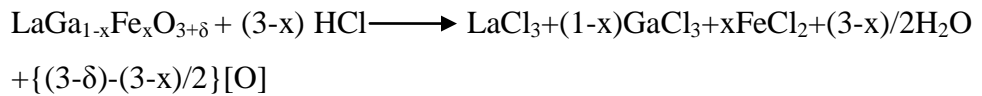
dielectric properties such as impedance, capacitance etc. due to electrodes. The dielectric measurements were carried out in the presence and absence of magnetic field as shown in fig.(2.8).

(d) Iodometric titration: In order to estimate the exact oxygen content in the prepared sample we have performed Iodometric titration, in case the value of the oxygen content deviates from the expected value i.e. 3 in the present case by some amount $\pm\delta$, this results in mixed valance state of Fe. Thus measuring oxygen content also provides information regarding the relative population of mixed valance state of Fe in the prepared samples. The details of titrations experiment are provided below.

Solutions preparation:

1. Dissolve 5.11525g of $\text{Na}_2\text{S}_2\text{O}_3 \cdot 5\text{H}_2\text{O}$ in 200 ml of water to make 0.10305N (normal) solution.
2. Prepare starch $((\text{C}_6\text{H}_{10}\text{O}_5)_n)$ solution by dissolving 1g of starch in 100ml of water.
3. Dissolve 1g of Potassium Iodide in 100 ml of water to prepare KI solution.

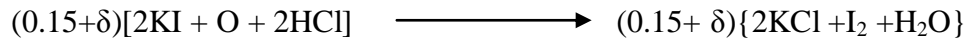
Principle: Here sample is dissolved in HCL and some volume of KI is used and reaction as follows:



For $x=0.3$,



(1.5+10 δ) nascent [O] oxygen is for 10 mole. So, for one mole sample (0.15+ δ) nascent oxygen will be formed.



Here $2(0.15 + \delta)I$ is used, so $2(0.15 + \delta)$ is the charge transfer during the reaction.

Now we use $Na_2S_2O_3 \cdot 5H_2O$ for titration and find the volume used to get end point.

Now,
$$N_1V_1 = N_2V_2 \quad \dots (2.8)$$

Where, N_1 , V_1 are normality and volume of sample and N_2 , V_2 are the normality and volume of $Na_2S_2O_3 \cdot 5H_2O$.

$$\begin{aligned} N_1V_1 &= \left(\frac{W_1}{W_{1eq} \times V_1} \right) \times V_1 \\ &= \frac{W_1}{\frac{Mol.Weight}{Chrgtransfer}} \\ &= \frac{W_1}{\frac{Mol.Weight}{2(0.15 + \delta)}} \\ &= \frac{W_1 \times 2(0.15 + \delta)}{Mol.Weight} \end{aligned}$$

Where, W_{1eq} is equivalent weight, W_1 is weight and Mol. Weight is molecular weight of sample.

Now, from equation (2.6)

$$\begin{aligned} \frac{W_1 \times 2(0.15 + \delta)}{Mol.Weight} &= N_2V_2 \\ \text{or, } \delta &= \frac{N_2V_2 \times Mol.Weight}{2W_1} - 0.15 \quad \dots(2.9) \end{aligned}$$

Working: After weighing sample about 0.1g dissolve it into HCl in a flask and add 10ml of KI solution, after being completely dissolved, it will become reddish. Now fill the burette with sodium thiosulphate and drop it drop by drop into the flask. The solution in the flask will become colorless (fig.2.9(4)) by following the sequence 1, 2, 3, 4 of fig. (2.9). Now add 2-3 drops of starch (indicator) it will become black (fig.2.9(6)), after adding some drops from burette it will again become colorless (fig2.9(5)). This is the end point of titration. This is the volume (V_2) and N_2 is already known,

by using equation 2.9 we can calculate δ and hence the charge states of element by using charge neutrality of compound.

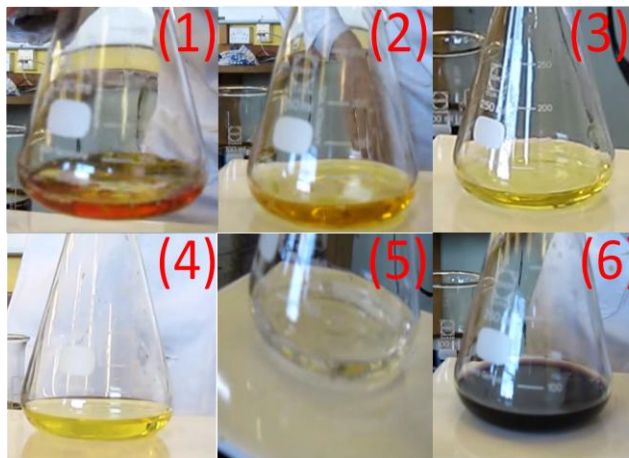


Fig. (2.9): Titration : Sequential step wise change in color up to end point.

(e) **X-Ray Absorption Near Edge Spectroscopy (XANES):** X-ray absorption technique is widely used to determine local geometric and/or electronic structure of matter. The experiment is usually performed at synchrotron radiation sources, which provide intense and tunable X-ray beams. Samples can be in the gas-phase, solution, or in solid state. X-rays are ionizing radiation and thus, by definition, have sufficient energy to eject a core electron from an atom. Each core shell has a distinct binding energy, and thus if one plots X-ray absorption as a function of energy, the spectrum for any atom resembles the X-ray absorption spectrum. When the X-ray energy is scanned through the binding energy of a core shell, there is an abrupt increase in absorption cross-section. This gives rise to a so-called absorption edge, with each edge representing a different core-electron binding energy. The edges are named according to the principle quantum number of the electron that is excited: K for $n=1$, L for $n=2$, M for $n=3$, etc. The core-electron binding energy increases with increasing atomic number, ranging from 284 eV for the C K edge to 115,606 eV for the U K edge, with the L edges at significantly lower

energies than the corresponding K edge. X-ray absorption spectroscopy (XAS) refers to the measurement of X-ray absorption cross-section in the vicinity of one or more absorbing edges.

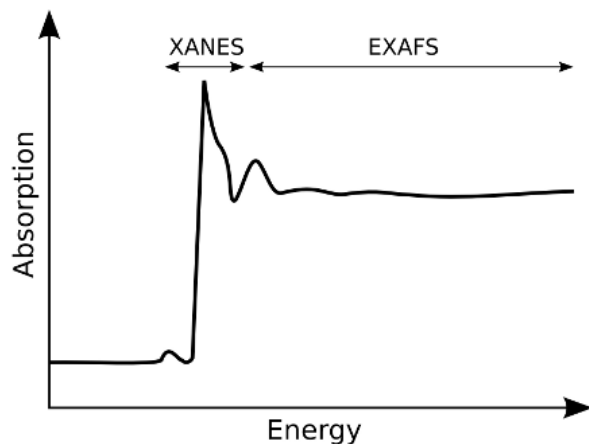


Fig.(2.10): X-ray absorption spectrum with XANES region.

The absorption spectrum of X-ray, is shown in fig. (2.10), which shows the absorption edge is not simply a discontinuous increase in absorption but in fact shows significant structure both in the immediate vicinity of the edge jump and well above the edge. The structure in the vicinity of the edge is referred to as XANES. There are several weak transitions below the edge, are called pre-edge transition, together with structured absorption on the high energy side of the edge which shows

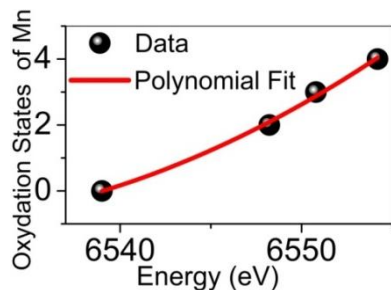


Fig.(2.11): The oxydation states of Mn references (i.e., 0, 2+, 3+ and 4+) as a function of the corresponding K-edge energies. The red curve is displaying a 2nd order polynomial fit of this data[18].

oscillatory behavior referred as EXAFS (not interested). By taking X-ray absorption spectrum of any sample with standard samples and extrapolating the curve between energy and charge state, charge state of sample can be calculated as shown in fig.(2.11).

Using these instrumental techniques we have characterized prepared samples and results are discussed in next chapter.

CHAPTER-3

Results and Discussions

Fe-doped polycrystalline samples are prepared as $\text{LaGa}_{1-x}\text{Fe}_x\text{O}_3$ ($x= 0.02, 0.04, 0.06, 0.08, 0.1, 0.15, 0.2, 0.25, 0.3, 0.4, 0.5, 0.6, 0.7, 0.8, 0.9, 1.0$) by solid state reaction method as discussed in chapter-2 with starting materials; La_2O_3 (99.99%), Ga_2O_3 (99.99%), and Fe_2O_3 (99.98%) and characterized, of which results are discussed in next three chapters.

3.1 Structural Studies (XRD)

XRD experiments were carried out on bruker D8 diffractometer equipped with Cu target to confirm the phase purity of the samples. Fig.(3.1.1) shows the powder XRD pattern of all prepared samples and the

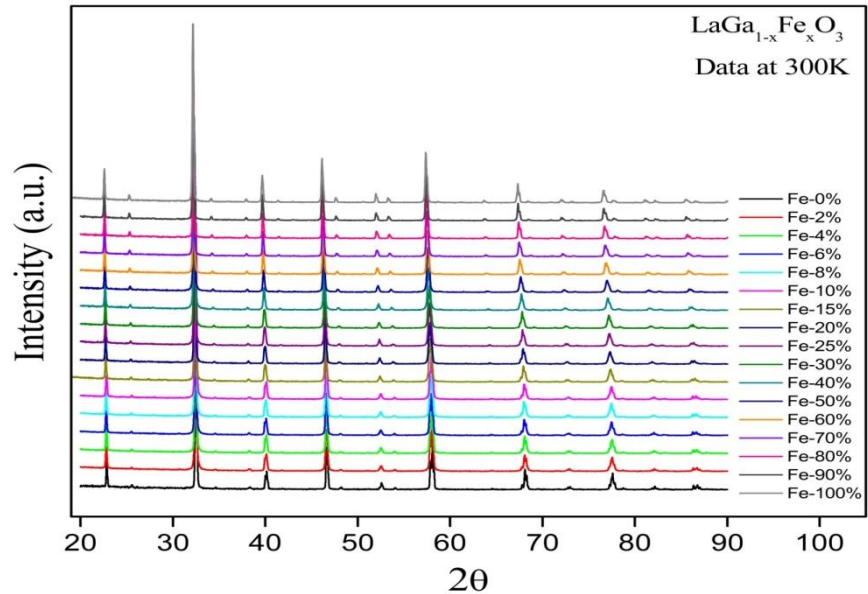


Fig.(3.1.1): Lab Source Room Temperature(RT) XRD Data of all Prepared Samples.

representative Rietveld refined diffraction data for $\text{LaGa}_{0.7}\text{Fe}_{0.3}\text{O}_3$ is shown in fig.(3.1.2) and it is one to one fit of experimental data (red

bubble) with simulated one (black line) is observed. This confirms the phase purity of sample as no obvious impurity peaks are observed.

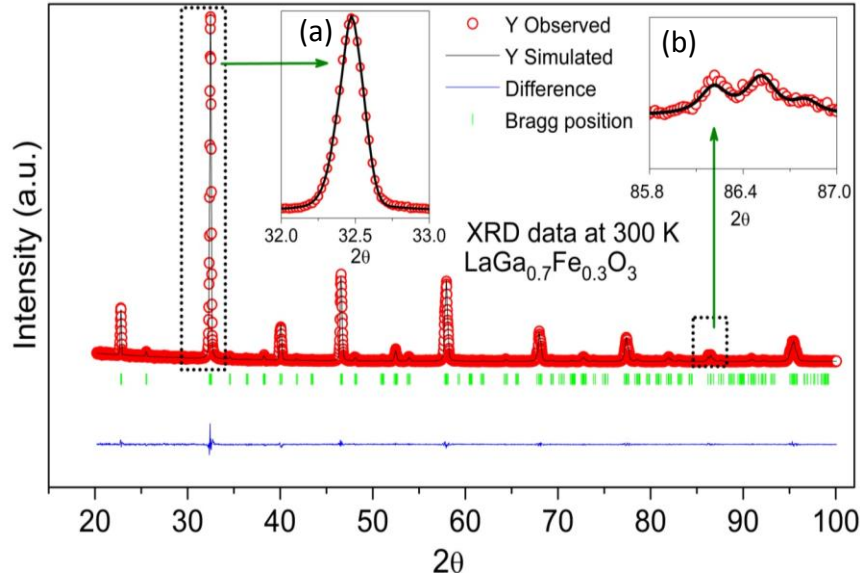


Fig.(3.1.2): Rietveld refined powder x-ray diffraction data for $\text{LaGa}_{0.7}\text{Fe}_{0.3}\text{O}_3$. The insets (a) and (b) show the magnified views for (121) at $2\theta = 32.45$ and (442) at $2\theta = 95.44$ respectively.

The diffraction data shown in fig.(3.1.1) shows the systematic shift towards lower 2θ value with Fe- doping. The same is shown in the inset (b) of fig.(3.1.3). Hence in order to estimate the value of lattice parameters with Fe doping we have used the 2θ values and calculated the lattice parameters. The value of lattice parameters due to Fe doping is shown in table (3.1.1). The increase in the value of lattice constant can be understood in the terms of difference in the ionic radii of Ga^{+3} (0.62) and Fe^{+3} (0.645)[32]. Also this increase in lattice constants enhances inter planar spacing-‘d’ and consequently diffraction angle θ decreases (according to Bragg’s condition $2d\sin\theta = n\lambda$). This corresponds to the shifting of Bragg’s peaks towards lower 2θ values. There exists a linear (or almost linear) variation of lattice parameters (3.1.4(1),(2),(3)) with Fe

doping; suggesting that the solid solution $\text{LaGa}_{1-x}\text{Fe}_x\text{O}_3$ follows the Vegard's law:

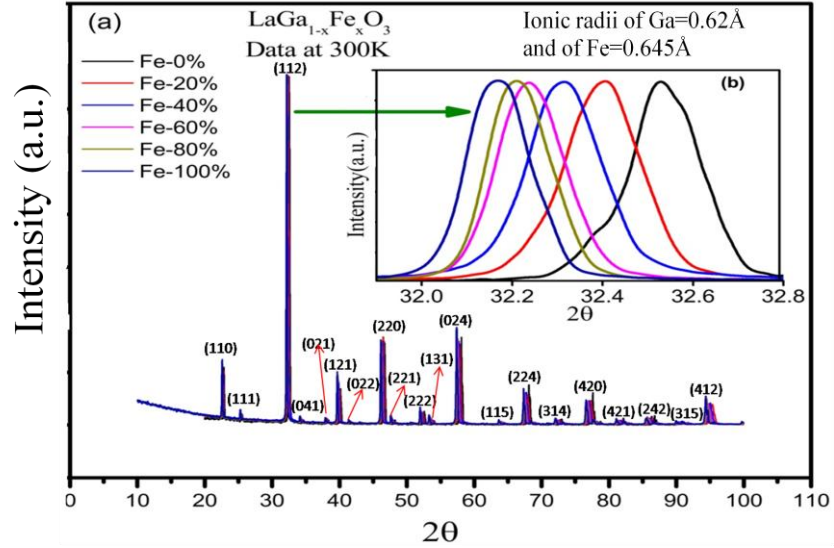


Fig.(3.1.3): (a) Lab source XRD data of $\text{LaGa}_{1-x}\text{Fe}_x\text{O}_3$ ($x=0.2, 0.4, 0.6, 0.8, 1.0$) and the the magnified view of (121) plane is shown in inset (b).

$$\mathbf{a}(\text{LaGa}_{1-x}\text{Fe}_x\text{O}_3) = \mathbf{a}(\text{LaGaO}_3)*(1-x) + \mathbf{a}(\text{LaFeO}_3)*(x)\dots(3.1.1)$$

Here $\mathbf{a}(\text{LaGa}_{1-x}\text{Fe}_x\text{O}_3)$ is the lattice parameter for x fraction of Fe doped sample; whereas $\mathbf{a}(\text{LaGaO}_3)$ and $\mathbf{a}(\text{LaFeO}_3)$ are the lattice parameters for pure LaGaO_3 and LaFeO_3 respectively. In order to confirm the same we have estimated the lattice parameters of intermediate samples using the lattice parameters of LaGaO_3 and LaFeO_3 by Vegard's law and compared the same with the experimentally observed lattice parameters; the same is shown in fig.(3.1.4(4),(5),(6)). The one to one (or almost one to one) match between the observed and calculated value of lattice parameter suggests that the solid solution $\text{LaGa}_{1-x}\text{Fe}_x\text{O}_3$ follows Vegard's law. Further from the fig.(3.1.4(4),(5),(6)) it is clear that the value of lattice parameter " \mathbf{a} "(fig.(3.1.4(4))) both experimental and as derived from Vegard's law matches well as compared to that of \mathbf{b} (fig.(3.1.4(6))) and \mathbf{c} (fig.(3.1.4(5))); this may be due to the possible room temperature orbital

ordering of Fe⁺³ and Fe⁺⁴ ions in *b-c* plane in the prepared samples[33–35] or due to the possible Jahn-Teller effect associated with Fe ion[36], it

Table (3.1.1): Values of lattice constants with Fe-doping.

Fe %(X)	Lattice Parameter a (Å)	Lattice Parameter b (Å)	Lattice Parameter c (Å)
2	5.494264	7.776982	5.526108
4	5.494871	7.777785	5.525634
6	5.495905	7.779399	5.525944
8	5.497052	7.781097	5.526467
10	5.498729	7.783417	5.527453
15	5.502085	7.788229	5.529192
20	5.505968	7.793382	5.531173
25	5.509290	7.797699	5.532521
30	5.513537	7.802872	5.534650
40	5.521674	7.812182	5.537574
50	5.529680	7.820450	5.541162
60	5.537786	7.828271	5.545008
70	5.544219	7.834773	5.548547
80	5.552273	7.842430	5.551383
90	5.558478	7.848284	5.553123
100	5.565476	7.853934	5.554533

needs further investigation. It should be noted that the near edge x-ray absorption spectroscopy (discussed in following section fig.3.3.10) and titration study confirms the presence of Fe in mixed (Fe⁴⁺ and Fe³⁺) valence state in the prepared samples. The presence of Fe in higher oxidation state may be termed as electron doping due to non-stoichiometric nature of Fe doped LaGaO₃ samples. Further Vegard's law

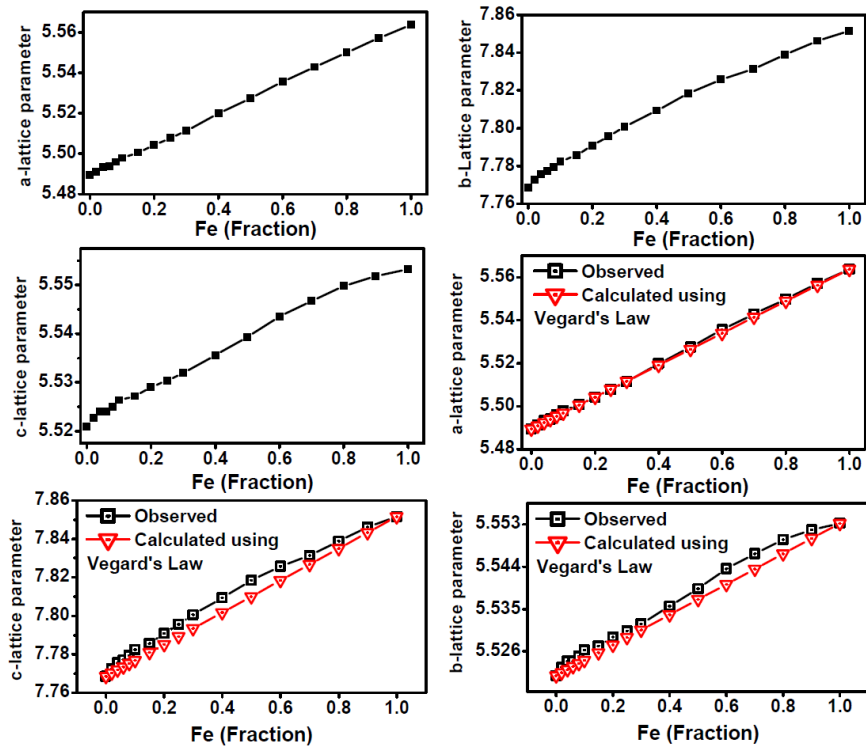


Fig.(3.1.4): Variation of lattice parameters as a function of Fe doping.

assumes isotropic/spherical expansion of unit cell but due to non-spherical shape of the atomic orbitals in most of the cases this assumption may not hold true.

3.2 Optical Properties Analysis

The optical band gap of prepared samples has been measured using diffuse reflectivity measurements. These measurements have been performed in the 190 nm to 800 nm wavelength range using Cary-60 UV-VIZ-NIR spectro photometer having Harrick Video-Barreline diffuse reflectance probe. The beam spot size on the sample was around 1.5 mm in diameter and an integral sphere detector is used for diffuse signal detection.

In order to estimate the optical band gap the diffuse reflectance spectra has been converted to equivalent absorption spectra using Kubelka–Munk equation (eq. 2.1)[25].

$$F(R_{\infty}) = \frac{K}{S} = \frac{(1 - R_{\infty})^2}{2R_{\infty}}$$

$$R_{\infty} = R_{\text{Sample}}/R_{\text{Standard}}$$

R_{Sample} is the diffuse reflectance of the sample and R_{Standard} is that of the standard (BaSO_4 in present case). K and S are the Kubelka–Munk absorption and scattering functions, respectively. As we have used powder samples for diffuse reflectance measurements, hence the assumption of reflected light scatters in a perfectly diffuse manner holds true, for such case the scattering function S is nearly constant with wavelength[37] and the Kubelka–Munk function can be related/proportional to the absorption coefficient (α) as eq.(2.2). Thus, a plot between $[F(R_{\infty}) \times hv]^n$ versus hv yields a straight line and the intercept on the energy axis gives the value of the band-gap. The value of $n = 2$ and $n = 1/2$, for direct and indirect band gap calculation respectively, has been taken to determine the optical gap of $\text{LaGa}_{1-x}\text{Fe}_x\text{O}_3$ as the doped LaGaO_3 is known to demonstrate excellent photoluminescence properties (which is a possible signature of direct band gap material)[15–17] whereas the first principle studies suggests that the indirect transition for these samples. Keeping this in view we have estimated the band gap considering both direct and indirect band gap. Tables-3.2.1 and 3.2.2 shows the band gap with different Fe- composition for $n=2$ and $n=1/2$ respectively. A plot between $[F(R_{\infty}) \times hv]^{1/2}$ and hv for various $\text{LaGa}_{1-x}\text{Fe}_x\text{O}_3$ is shown in fig.(3.2.1). It is clear that band- gap around 3.50eV and 2.50eV is more prominent in less doping of Fe and with higher doping of Fe, it decreases and become more prominent around 2.50eV and 2.10eV. Also a plot between $[F(R_{\infty}) \times hv]^2$ and hv is shown in fig.(3.2.2). It is clear that band gap around 3.40eV and 2.45eV is more prominent in less doping of Fe and gap around 2.50eV and 2.20eV is more prominent in higher doping of Fe. This change in the band gap with Fe doping is due to the change in lattice parameter with Fe doping at Ga site, due to which the diffraction of electrons at potential boundary will change

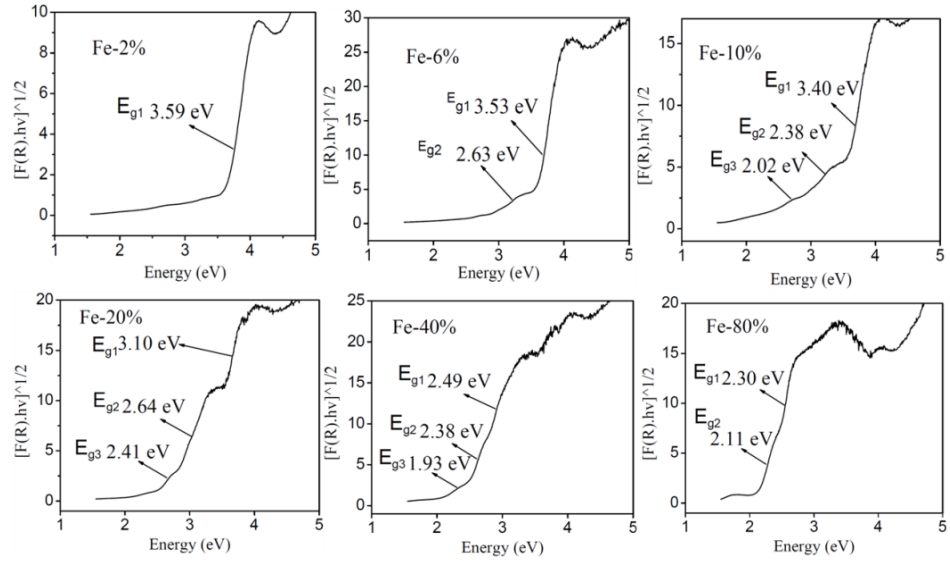


Fig.(3.2.1): The equivalent Tauc plot for indirect band-gap of $LaGa_{1-x}Fe_xO_3$ samples.

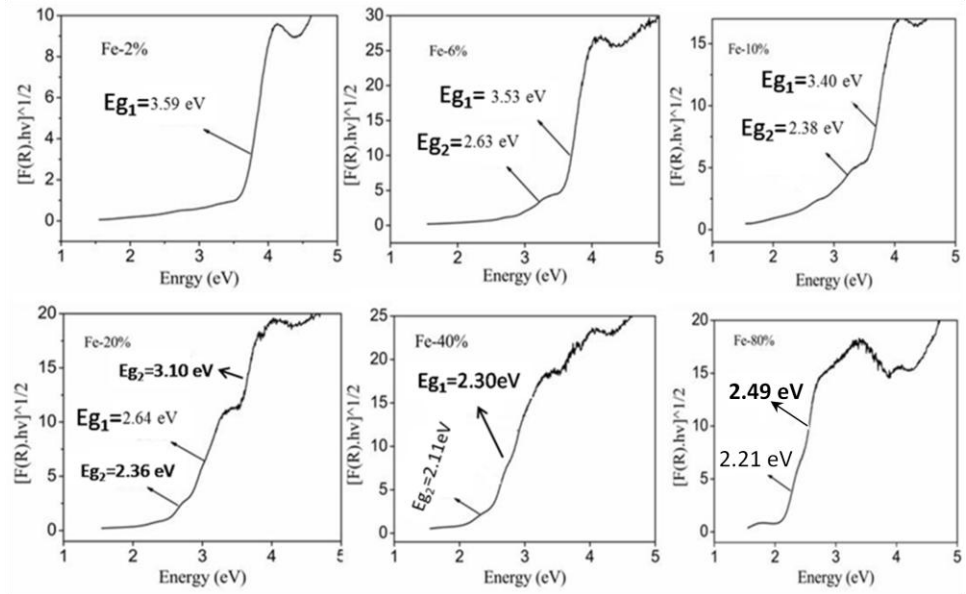


Fig.(3.2.2): The equivalent Tauc plot for direct band-gap of $LaGa_{1-x}Fe_xO_3$ samples.

according to Kronig-Penney model. The occurrence of new energy states at low energy side with doping may be understood either in the terms of electron/hole doping or due to defects (vacancies) present in the sample [38–40]. In order to understand the occurrence of new low energy

states in the Fe doped samples we have carefully examined the valency of Fe in $\text{LaGa}_{1-x}\text{Fe}_x\text{O}_3$. Using XANES[41] as discussed below. From XANES data (discussed below) it is clear that fraction of Fe is other than

Table(3.2.1): Indirect Band-gaps with Fe-Composition. Here E_{g1} and E_{g2} are corresponding to two different absorption edges (see fig.3.2.1).

% Fe	E_{g1} (eV)	E_{g2} (eV)	E_{g3} (eV)	% Fe	E_{g1} (eV)	E_{g2} (eV)	E_{g3} (eV)
0	3.90		-	30	2.59	2.39	1.80
2	3.59		-	40	2.49	2.38	
4	3.54	2.67	-	50	2.37	1.96	-
6	3.53	2.63	-	60	2.40	2.08	-
8	3.43	2.35	2.01	70	2.36	2.09	-
10	3.40	2.38	2.02	80	2.30	2.11	-
15	3.29	2.67	2.43	90	2.20	2.10	-
20	3.10	2.64	2.41	100	2.10		-
25	2.85	2.58	2.36				

+3 state or oxygen is other than 3 i.e. $(3\pm\delta)$. It is also verified by performing iodometric titration experiments that samples are not in proper stoichiometry (i.e. O is $3\pm\delta$). Due to which defect states may be created between valence band and conduction band region or due to the orbital overlapping new states may be created, as shown in fig.(3.2.3(b)). The signature of transition due to defect states/orbital overlapping will also be present in DRS experiment. Hence different new transitions are possible (fig.3.2.3). The δ is different for different composition of Fe, thus defects states/orbital overlapping may also be different for different composition of Fe. So due to defect states/orbital overlapping low energy transitions will occur and the signature of lower band gap with doping of Fe is present. This property may be one explanation for generation of new intensity peaks at lower energy side with doping of Fe. Fig.(3.2.4) shows

Table(3.2.2): Direct Band-gaps with Fe-composition. Here E_{g1} and E_{g2} are corresponding to two different absorption edges (see fig.3.2.2).

%Fe	E_{g1} (eV)	E_{g2} (eV)	%Fe	E_{g1} (eV)	E_{g2} (eV)
0	4.01	-	30	2.71	2.52
2	3.75	-	40	2.45	2.35
4	3.68	-	50	2.47	2.15
6	3.64	-	60	2.48	2.21
8	2.87	3.60	70	2.48	2.20
10	3.52	2.78	80	2.49	2.21
15	3.27	2.86	90	2.48	2.19
20	3.10	2.50	100	2.50	2.19
25	2.90	2.53			

the variation of band gap as a function of Fe doping for direct (fig.3.2.4(a)) and indirect (fig.3.2.4(b)) band-gaps. From the fig.(3.2.4) it is clear that with increase in Fe doping in $\text{LaGa}_{1-x}\text{Fe}_x\text{O}_3$ the optical band gap gradually decreases and attains the saturation value of $\sim 2.1\text{eV}$ at $x = 0.4$. The data shown in the fig.(3.2.4) is fitted to estimate the value of bowing parameter using equation:

$$E_{g[\text{LaGa}_{1-x}\text{Fe}_x\text{O}_3]} = (1-x) * [E_{g:\text{LaGaO}_3}] + x * [E_{g:\text{LaFeO}_3}] - b *(x) * (1-x) \dots (3.2.1)$$

Here, $E_{g:\text{LaGaO}_3}$ and $E_{g:\text{LaFeO}_3}$ are the optical gaps of LaGaO_3 and LaFeO_3 and b is the bowing parameter. The value of $E_{g:\text{LaGaO}_3}$ for orthorhombic structure is 3.9eV using indirect band-gap calculation and 4.02eV using direct band gap calculation and of $E_{g:\text{LaFeO}_3}$ is 2.10eV using indirect band-gap calculation and 2.19eV using direct band-gap calculation and these are in good agreement with the values reported in the literature[42]. We have fitted the experimental optical gap data using equation (3.2.1) as shown by the dotted line in fig(3.2.4). The best fit was obtained for a bowing parameter value of $+3.59 \pm 0.14\text{eV}$ for direct band-gap and $+3.43 \pm 0.23\text{eV}$ for indirect band-gap calculation. Which shows a strong overlapping between 3-d of Fe and 2-p of O orbital.

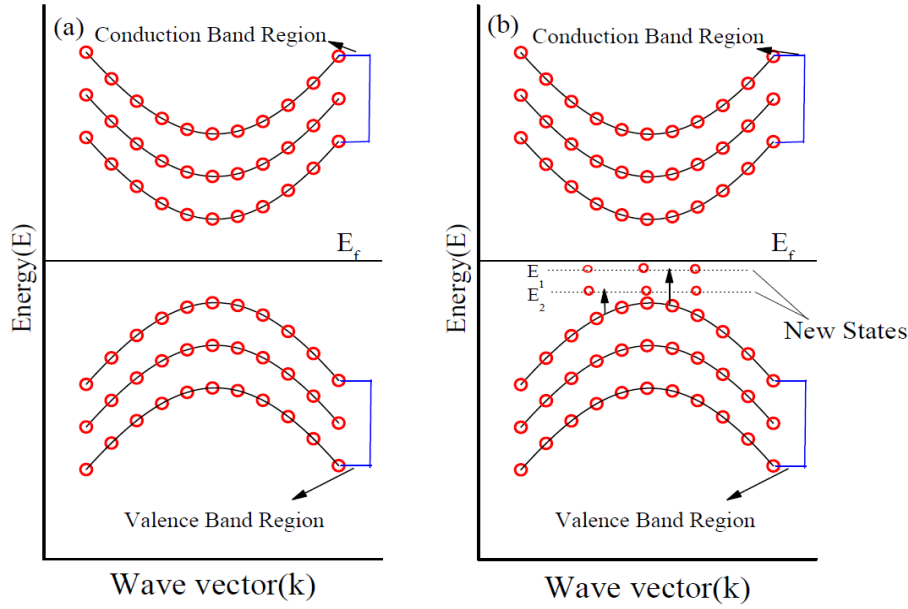


Fig.(3.2.3): (a) Intrinsic band-diagram of solids and (b) Band-diagram of solids due to orbital overlapping.

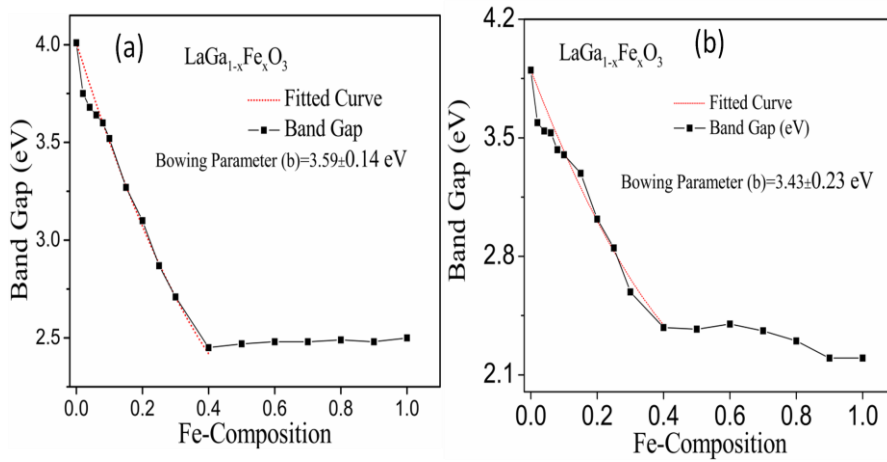


Fig.(3.2.4): (a) Fitting of band- gap for Bowing parameter calculation using direct band gap and (b) Fitting of band- gap for Bowing parameter calculation using indirect band gap.

3.3 Dielectric and Magneto-dielectric Properties

Dielectric Properties: For dielectric measurements single phase powdered samples were pelletized at a high pressure of 15 ton to form 1 mm thick circular discs of 12 mm diameter and these pellets were sintered in air at 1300°C for 24 hours. The dielectric properties of prepared pellets have been measured at room temperature for a frequency range of 20Hz to 10 MHz by using Wynne Kerr 65120B precision impedance analyzer with an oscillator voltage of +1 volt. The dielectric constant of the prepared samples is estimated by measuring the capacitance and geometry of the prepared samples. The variation of the dielectric constant of some samples as a function of Fe and frequency is shown in fig. 3.3.1(a) and the corresponding dielectric loss is shown in fig. 3.3.1(b). From the figure it is clear that dielectric constant is increasing with Fe doping and also the

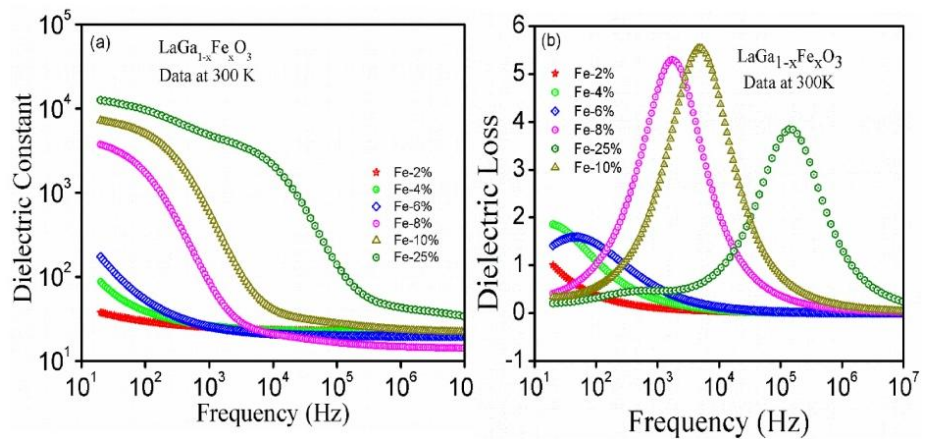


Fig.(3.3.1): The behavior of dielectric constant (a) and dielectric loss of $LaGa_{1-x}Fe_xO_3$ (for some value of x) as a function of frequency and Fe composition.

corresponding dielectric loss almost increasing with Fe doping. Further from fig. 3.3.1(b), it is clear that when Fe doping exceeds 4%, a peak in dielectric loss ($\tan(\delta)$) appears and this peak systematically shifts towards higher frequency side with Fe doping. The peak in $\tan(\delta)$ suggests the presence of dielectric relaxation in the prepared samples[43]. The variation of dielectric constant with Fe doping may be understood by

carefully looking in to the real and imaginary values of impedances of the prepared samples. Fig 3.3.2 represents the Cole-Cole (Nyquist) plot for the studied samples. From fig.3.3.2 (sections a and b) it is clear that with the increasing Fe concentration, the maximum value of both the real and imaginary parts of impedance decreases by in orders of magnitude at higher frequency side, this suggests that the AC conductivity of the prepared samples increases as a result (considering effective medium approach) increase in the value of dielectric constant is observed possibly due to apparent decrease in the thickness of the sample[18]. In the case of Fe based samples (Ferrites) it is reported that the presence of Fe in mixed valence state leads to increase in AC conductivity and dielectric loss in the sample. Hence in order to investigate the valency of Fe in the prepared samples the x-ray near edge spectroscopy experiments were performed as discussed below. From XANES data as well as from Iodometric titration experiment, it is clear that Fe is in mixed valence Fe^{+3} and Fe^{+4} state in the prepared samples. With increase in Fe doping the numbers of Fe^{+3} and Fe^{+4} sites increases which lead to increase in the AC conductivity. The frequency response of $\tan(\delta)$ i.e. shifting in the peak of $\tan(\delta)$ may be understood on the basis of the dipolar effect and hopping of charge carrier (polaron in the present case as Fe^{+4} is a Jahn-Teller ion) between Fe^{+3} and Fe^{+4} ions[18]. The shifting in the peak of $\tan(\delta)$ may be understood considering cole-cole relaxation process.

$$\varepsilon(\omega)^* = \varepsilon_{\infty} + \frac{\varepsilon'_s - \varepsilon'_{\infty}}{1 + (i\omega\tau)^{1-\alpha}}; 0 \leq \alpha \leq 1$$

Here $\varepsilon(\omega)^* = \varepsilon' + i\varepsilon''$ is the complex dielectric permittivity, ε'_s and ε'_{∞} are the values of the dielectric constant in the low-frequency (static) and high-frequency limit respectively, τ is the mean relaxation time, ω is the angular frequency, the change $\varepsilon'_s - \varepsilon'_{\infty} = \Delta\varepsilon'$ is the strength of dielectric relaxation and α is the exponent parameter which is accounted to the relaxation

broadening and it varies between 0 and 1; for $\alpha=0$, cole-cole expression (3.3.2) reduces to Debye single relaxation process[44]. It is observed that

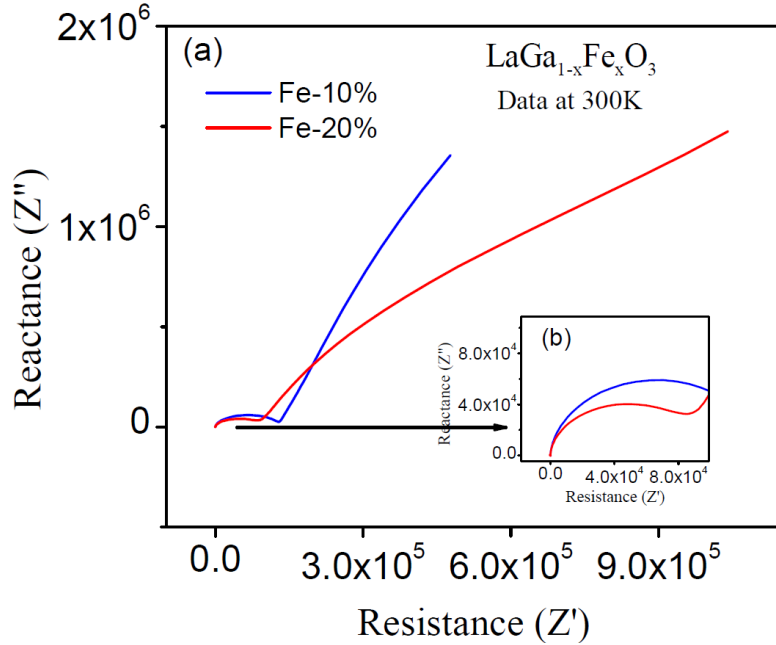


Fig.(3.3.2): (a) Cole-cole diagram Fe- doped LaGaO_3 for whole probing frequency and (b) the enlarged version of cole-cole diagram at higher frequency.

the value of τ decreasing with Fe doping which suggests increase in the value of average hopping frequency between Fe^{+3} and Fe^{+4} sites with Fe doping. This may be the reason for shifting in the peak of $\tan(\delta)$ towards higher frequency side with increase in Fe doping. At this juncture it is important to note that recently we have reported detail dielectric studies on Mn doped LaGaO_3 samples[18]. As the dielectric behaviour for Fe doped samples (present results) are analogous to that of Mn doped samples, hence for detail dielectric analysis we encourage the reader to look in to our results reported for Mn doped LaGaO_3 [18].

Magneto Dielectric(MD) Properties: For magneto-dielectric measurements single phase powdered samples were pelletized at a pressure of 15 ton to form 1 mm thick circular discs of 12 mm diameter and these pellets were sintered in air at 1300°C for 24 hours. Further, after being coated with silver paint these pellets were fired at 300°C for 30 min.

The RT (room temperature) capacitance along with the frequency dependent magneto resistance or MR (FDMR) i.e. change in real part of impedance, for all prepared pellets is measured in the absence and

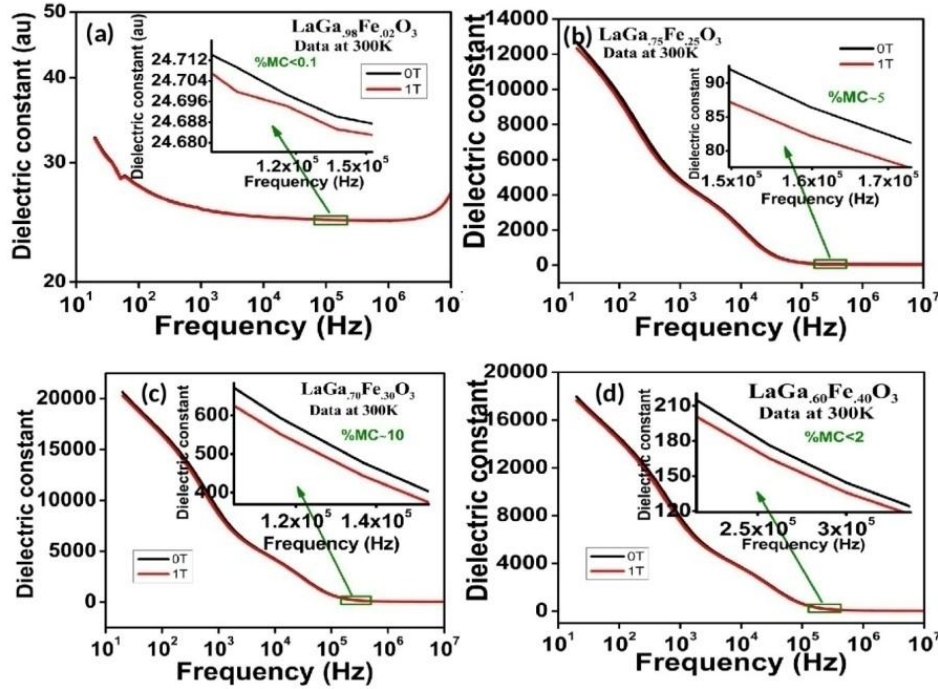


Fig.(3.3.3): Change in dielectric constant of $LaGa_{1-x}Fe_xO_3$ ($x=0.02,0.25,0.30,0.40$) with the application of magnetic field ($H=1T$).

presence of magnetic field by using a Wynne Kerr 65120B precision impedance analyzer with an oscillator voltage of $\pm 1V$ and at operating frequencies ranging between 20 Hz to 10 MHz. The direction of applied magnetic field was kept along the ac electric field to ensure the complete absence of contributions which may arise in MD measurements due to Hall-effect geometry. The resistivity and magneto-resistance measurements (dc MR) were carried out at magnetic field of 0 T and 0.7 T in standard four-probe geometry using Keithley 2182A Nano voltmeter and 6221 source meter.

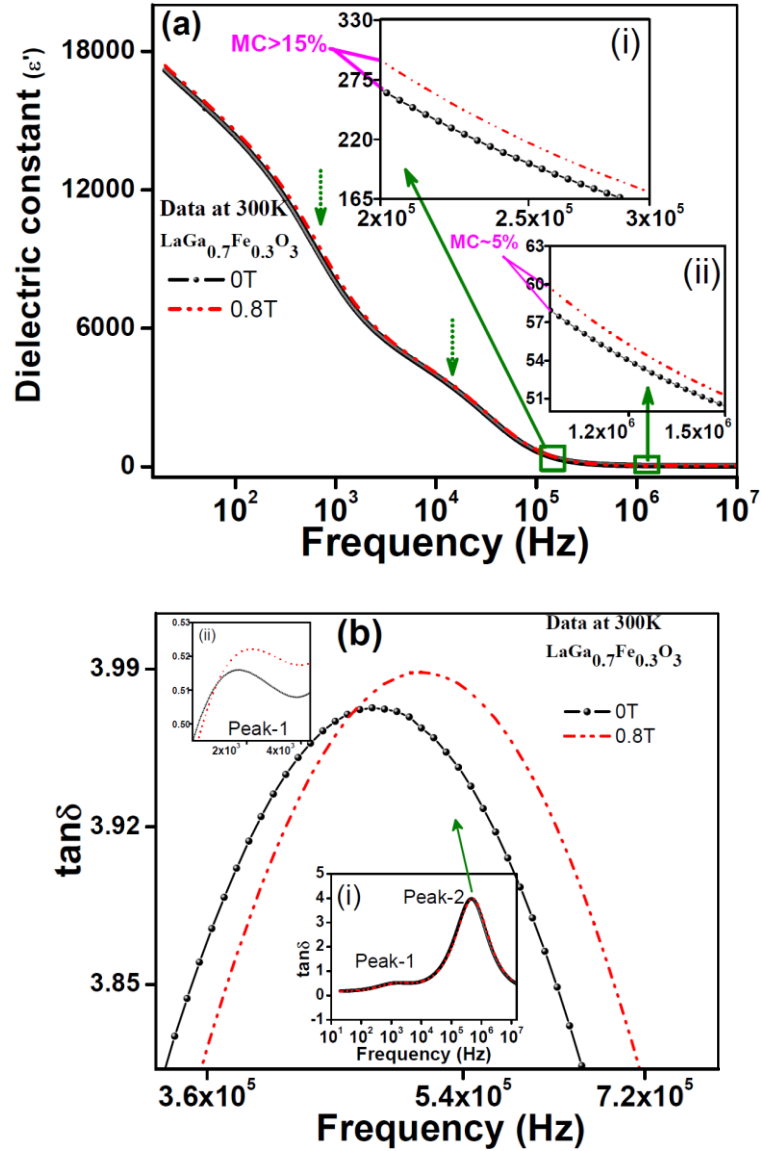


Fig.(3.3.4): Room-temperature (a) dielectric constant (ϵ') and (b) dielectric loss ($\tan\delta$) as a function of frequency measured in the absence ($H=0.0$ T) and presence (0.8 T) of magnetic field for $\text{LaGa}_{0.7}\text{Fe}_{0.3}\text{O}_3$. In (a), insets show magnified view of data at corresponding frequency ranges. In (b) the data corresponding to entire range of probing frequencies is shown in the inset (i) and high frequency data is magnified as main panel for clarity. The inset (ii) displays magnified view of first broad peak.

Fig.(3.3.3) shows the change in the dielectric constant of $\text{LaGa}_{1-x}\text{Fe}_x\text{O}_3$ (for some value of x) with application of magnetic field. It is clear from the figure that the change for less doping is small and we are getting

a huge change (>10%) in dielectric constant for $x=0.3$ even at higher frequency side. To confirm that this change in dielectric constant is intrinsic property, further different parameters were studied for $x=0.3$, as discussed below. Fig.(3.3.4) (a) and (b) show the RT frequency dependence of ϵ' and dielectric loss ($\tan\delta$) respectively for $\text{LaGa}_{0.7}\text{Fe}_{0.3}\text{O}_3$ (LGFO). These measurements were carried out in the absence ($H=0$ T) and presence of magnetic field of 0.8 T over the entire range of probing frequency (20 Hz to 10 MHz). It is clear that a noticeable change (upsurge) in the value of ϵ' is observed throughout the entire probing frequency range due to the application of a magnetic field of 0.8T. This observed MD effect is strong at low frequencies and significant even at higher probing frequencies. Interestingly, ~100 kHz this observed change is found to be >15% for a magnetic field of $H=0.8$ T which is huge in compare to the MD effect reported by others at same/lower probing frequency in different materials[45–49] but, with the application of similar[45]/relatively higher magnetic field[45,46,48,50]. Inset (ii) shows that the change is ~5% even at a high frequency of 1 MHz with $H=0.8$ T. This change in the value of RT ϵ' due to the application of magnetic fields are tabulated in table 3.3.1 for probing frequencies of 100 kHz and 1 MHz respectively. It should be noted that this observed change in ϵ' (measured at various frequencies and with the application of different magnetic fields) is well above the sum of instrumental and statistical error bar. Moreover, $\tan\delta$ also increases over the entire range of probing frequency due to the application of magnetic field as it is shown in fig.3.3.4 (b), its inset (ii) and fig. (3.3.5) by magnifying the corresponding frequency ranges. Further, two broad peaks have also been observed in $\tan\delta$ which are indicated as peak-1 and peak-2 as shown in the inset (i) of fig. 3.3.4(b). Peak-1 is prominent in height whereas peak-2 is relatively much broader. These characteristic $\tan\delta$ -peaks are corresponding to the diffusive anomalies in ϵ' (indicated by two dotted down arrows in the fig. 3.3.4 (a))observed across the same range of probing frequencies. These two

peaks (diffusive anomalies) in $\tan\delta(\epsilon')$ indicate the presence of two dielectric relaxation processes in presently studied LGFO samples and it

Table-3.3.1: Change observed in the value of room temperature ϵ' (in %) due to the application of magnetic fields of 0.2 T and 0.8 T.

Frequency	% Change observed in the value of room temperature ϵ' due to the application of different magnetic fields	
	0.2 T	0.8 T
100 kHz	1.74	9.13
1 MHz	0.59	2.99

may be interesting to explore them in future from relaxation perspective. Ultimately, following four major observations (considering MD phenomenon) are noticeable from fig.3.3.4 (a) and (b) – (i) a significant RT MD effect is appearing at application of magnetic field. (ii) Both ϵ' and $\tan\delta$ are increasing with increasing magnetic field over entire range of probing frequencies. This same trend indicates that the observed with field RT MD effect is an intrinsic property of LGFO sample with $x=0.3$ as also suggested[51] /pointed out[45] /shown[45,46,49] by others. (iii) the peak positions of both broad $\tan\delta$ -peaks are clearly visible to be shifted towards higher frequency side with the application of magnetic field which points towards the magneto resistive origin (negative dc MR)[51] of presently observed RT MD phenomenon as proposed by G. Catalan[51] and (iv) $\tan\delta$ is increasing due to the increasing magnetic field even at the frequencies $>10^6$ Hz (fig. 3.3.5) which might be appearing either due to the increased leakage through conduction electrons or due to the mismatch of applied ac frequency with that of the frequency of dipolar oscillations associated with the flipping of a dynamic ‘ $\text{Fe}^{4+}/\text{Fe}^{3+}$ ’ dipole/a natural dipole originated due to off-centrosymmetry around central transition metal (TM) ion in $(\text{TM})\text{O}_6$ octahedron[18] or due to both of them. It is to

be noted that the oxygen stoichiometry and the coexistence of Fe charge states i.e. Fe^{4+} and Fe^{3+} in the present $\text{LaGa}_{0.7}\text{Fe}_{0.3}\text{O}_{3\pm\delta}$ sample is established by using iodometric titration as well as XANES (as discussed below) experiments[52]. Our titration experiments reveal oxygen efficiency in present LGFO sample as the value of δ is found to be +0.043. Further, with this value of δ , percentage of 4^+ and 3^+ charge states in total Fe present in LGFO sample has been calculated by using the charge neutrality condition and as a result 29% of total Fe is found to be present in 4^+ state whereas remaining 71% is Fe^{3+} . However, besides the same

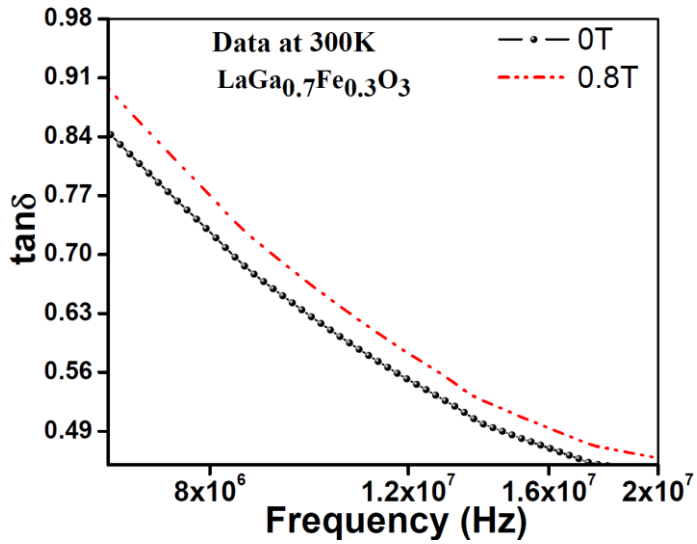


Fig.(3.3.5): Room-temperature loss tangent ($\tan\delta$) as a function of frequency measured in the absence ($H= 0.0 \text{ T}$) and presence (0.8T) of magnetic field. The data is shown only for higher frequencies to demonstrate that the value of $\tan\delta$ increases with increasing magnetic field even at the frequencies of $> 1 \text{ MHz}$ and its value remains < 1 even at such high frequencies.

trend of change observed in ϵ' and $\tan\delta$ due to magnetic field, the trends observed in MC% and ML% (both increase with increasing magnetic field at high frequencies $\geq 1\text{MHz}$ as shown in Fig. 3.3.6 (a) and (b)) also suggest that the presently observed low field RT MD effect should be an intrinsic nature of presently studied $\text{LaGa}_{0.7}\text{Fe}_{0.3}\text{O}_3$ sample at frequencies 100Hz, 100kHz and 1MHz as the same is proposed by G. Catalan[45,51].

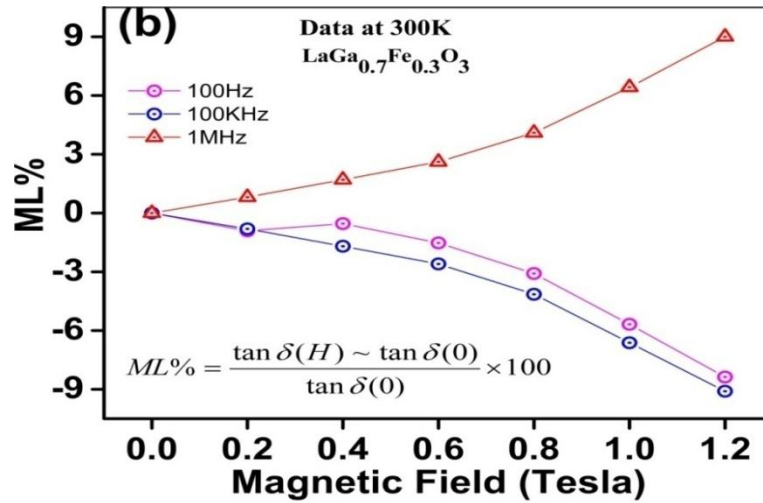
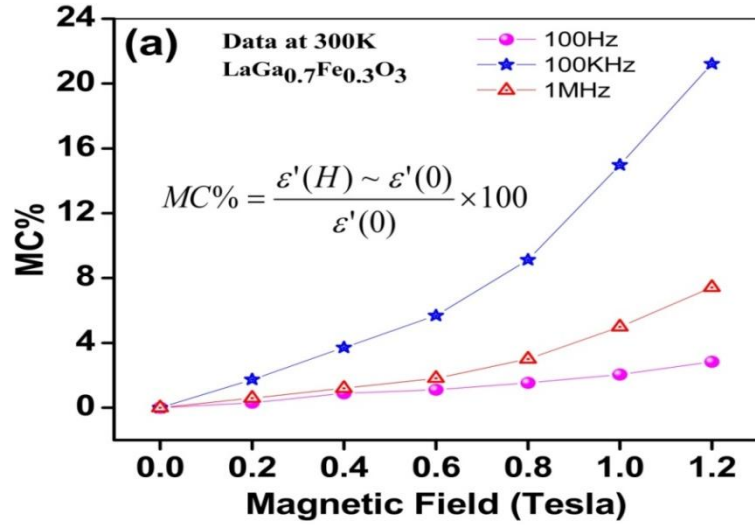


Fig.(3.3.6): The trends of Room-temperature (RT) -(a) Magneto-capacitance (MC%) and (b) Magneto-loss (ML%) as a function of applied magnetic fields for LaGa_{0.7}Fe_{0.3}O₃ measured at selected frequencies from 100 Hz to 10 MHz. Both MC% and ML% are increasing with magnetic field for probing frequency of $\geq 10^6$ Hz. On the other hand at frequencies $< 10^6$ Hz MC% and ML% are changing oppositely due to increasing magnetic field. Both MC% and ML% have been calculated by using the formulae shown in corresponding figures. Where, $\varepsilon'(0)$ and $\varepsilon'(H)$ are the dielectric constant correspondingly in the absence ($H=0.0$ T) and presence of magnetic field ($H=0.8$ T) whereas $\tan\delta(0)$ and $\tan\delta(H)$ represent loss tangent respectively in the absence ($H=0.0$ T) and presence of magnetic field ($H=0.8$ T).

On the other hand, at frequencies $< 1\text{MHz}$ the effect appears to be MR dominated as the trends observed in MC% and ML% are opposite at these

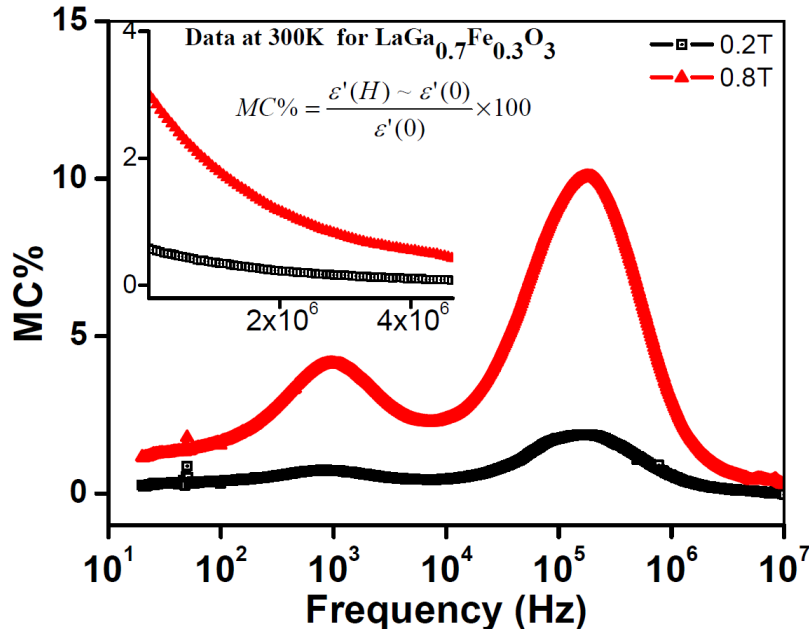


Fig.(3.3.7): Room-temperature MC% as a function of probing frequency for different magnetic fields. Inset displays MC% data at higher frequencies ($\geq 10^6\text{Hz}$) to show that the observed MD effect is significant even at such high frequencies also. MC% has been calculated by using the formula shown in figure. Where, $\epsilon'(0)$ and $\epsilon'(H)$ are the dielectric constant correspondingly in the absence ($H=0.0\text{ T}$) and presence of magnetic field ($H=0.8\text{ T}$).

frequencies (MC% is increasing and ML% is decreasing with increasing magnetic field). Moreover, as depicted in fig.(3.3.7), two broad peaks in the MC% vs frequency plot have also been observed across the frequencies high frequencies $\geq 1\text{MHz}$ as shown in fig.3.3.6 (a) and (b)) also corresponding to peaks (diffusive anomalies) in $\tan\delta(\epsilon')$ for all values of applied magnetic fields. The MC% is found to be increased with increasing magnetic field even upto MHz frequencies (inset of fig. 3.3.7) i.e. over the entire range of probing frequencies. Further, the position of both the broad MC% peaks appears to be almost unaltered due to the application of magnetic field of 0.8T. However, a careful analysis revealed that the frequency corresponding to MC% maximum changes with applied

magnetic field; the same is tabulated in table 3.3.2. This points towards the possibility of field-induced dipoles as an origin of presently observed RT MD effect in LGFO sample with $x=0.3$ as Chandrasekhar et al[53] have suggested that - to ruled out the possibility of field-induced dipolar relaxation, the said MC% peak position should not be changed with the application of magnetic field. Now, in order to further examine that whether the presently observed MD effect is MR dominated or it is an intrinsic behavior of the sample under study, firstly RT dc MR has been

Table-3.3.2: The frequencies (Hz) corresponding to maximum value observed in broad peak of MC% for the magnetic fields of 0.2 T and 0.8 T.

Broad peak of MC%	Frequency (Hz) corresponding to maximum value observed in broad peak of MC% for different magnetic fields	
	0.2 T	0.8 T
Peak-1	0.85×10^3	0.96×10^3
Peak-2	1.63×10^5	1.80×10^5

measured by means of I-V measurements as plotted in fig. (3.5.8). A small positive dc MR has been observed as the voltage across each value of current is found to be slightly increased due to increasing magnetic field as shown in I-V performed in the absence ($H=0.0$ T) and presence of magnetic field (0.7 T) to measure real (Z') and imaginary (Z'') part of impedance. The data of these MRIS measurements for $\text{LaGa}_{0.7}\text{Fe}_{0.3}\text{O}_3$ sample is shown as a Cole-Cole (Nyquist) plot[18,54] in fig.(3.3.9). It is clear from fig. 3.3.9 (a) and (b) that at the frequencies corresponding to space charge and grain boundary contributions i.e. at low and mid-range of probing frequencies (20 Hz to $<10^6$ Hz), the value of both Z' (resistance) is decreasing significantly due to the application of magnetic

field which suggests that the large MD effect observed at these frequencies (fig. 3.3.4(b)) is FDMR affected/dominated. This analysis

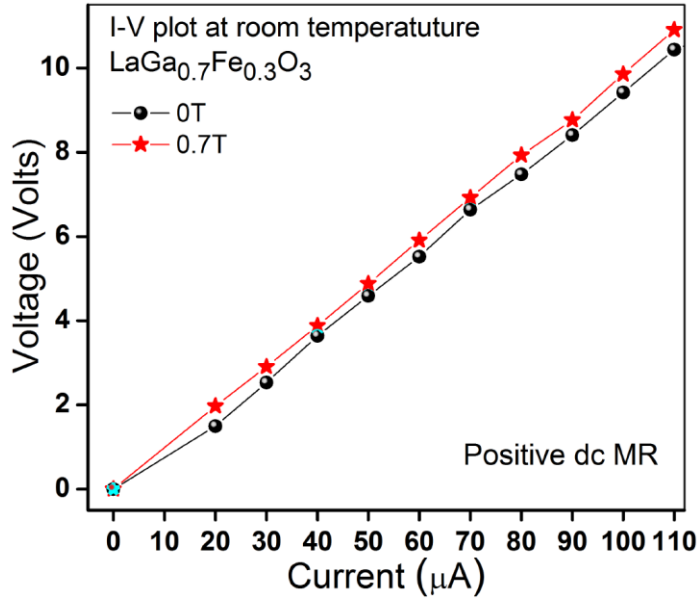


Fig.(3.3.8): Room temperature I-V plot drawn by measuring the voltage for different values of current in the absence ($H=0.0$ T) and presence ($H=0.7$ T) of magnetic field by using standard four-probe method.

reveals that the shifting of $\tan\delta$ -peak position towards higher frequency due to applied field can be credited to negative FDMR. This FDMR can be attributed to the hopping of electrons between Fe^{4+} and Fe^{3+} via intermediate oxygen by following the double exchange mechanism as the magnetic field makes this exchange easier[41] and consequently Z' decreases (negative FDMR) which appears to be responsible (along with non-intrinsic interface effects; arises due to the accumulation of free charges at interface between different grains within the bulk itself and at the electrode-sample interface which are recognized as Maxwell-Wagner and space charge polarizations respectively) for presently observed large (significant) MD effect at low (mid) frequencies. Moreover, as the magnetic field makes the said exchange easier, therefore, the dynamic dipole ($\text{Fe}^{4+}/\text{Fe}^{3+}$) starts oscillating with a higher frequency (as also

explained previously for ‘Mn³⁺/Mn⁴⁺’ dipole in Mn doped lanthanum gallate[18]) and hence tanδ-peak(s) corresponding to this characteristic

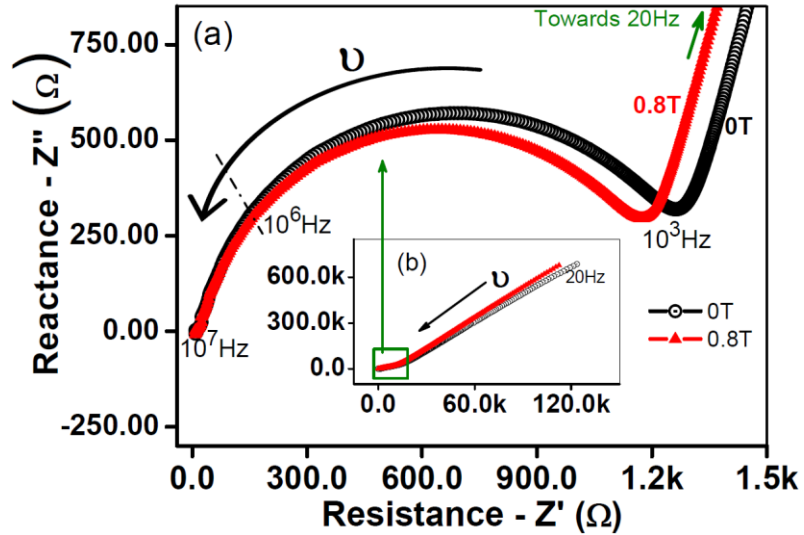


Fig.(3.3.9): Room-temperature Cole-Cole diagram of $LaGa_{0.7}Fe_{0.3}O_3$ plotted for frequencies ranging between 20 Hz to 10 MHz is shown in inset (b) and only high frequency data is magnified as main panel in (a). The data is measured in the absence ($H=0$ T) and presence of magnetic field (0.8 T).

frequency is (are) observed to be shifted towards higher frequency side due to the presence of magnetic field (fig. 3.3.4(a)). However, the MD effect is expected to be intrinsic when it is measured at probing frequencies higher (presently ≥ 100 kHz) to characteristic frequency[51] (the frequency of electron hopping between Fe^{4+} and Fe^{3+}) because at such high frequencies the hopping charge transport (ultimately MR) gets suppressed as the carriers have no chance to jump between hopping sites[18,51,55] (presently Fe^{4+} and Fe^{3+}), therefore, only grain contribution is expected with a low value of $\tan\delta$ [18,55] (presently 10^{-1}) as shown in the fig. (3.3.5). Further, at frequencies corresponding to grain contributions ($\geq 10^6$ Hz), neither part of impedance is changing due to the application of magnetic field which discards any contribution of MR (dc/FD) in the observed MD coupling at these high frequencies (fig. 3.3.4

and Table 3.3.1). It also suggest that at these high frequencies the change observed in $\tan\delta$ (fig. 3.3.5) due to application of magnetic field is not arising due the leakage through conduction electrons and may be attributed solely to the mismatch of applied ac frequency with that of above discussed dipolar oscillations. Now as whole regardless of probing frequencies, the observed RT MD appears to be an intrinsic nature of presently studied LGFO sample though it is FDMR (along with other possible extrinsic effects) dominated at frequencies $<10^5$ Hz. The intrinsic contribution of presently observed RT MD coupling can be attributed to magneto-striction phenomenon[55,56] associated with the change in the lattice parameters or bond angles due to the magnetic field induced strain which can be explored in detail to confirm our speculation. In this regard, we propose that it will be interesting to study magnetic field dependent structure of the studied LGFO samples at different temperatures. Ultimately, present study suggests that Fe doped LGO may be a good RT MD material.

To confirm the charge state of the samples, we have performed X-Ray Near Edge Spectroscopy (XANES) experiment as shown in fig.(3.3.10). Fig.(3.3.10) shows the XANES spectra for the studied samples along with that of FeO (Fe^{+2}) and Fe_2O_3 (Fe^{+3}) standards. The energy axis is calibrated using pure Fe foil as standard and the value of the absorption edge is estimated by taking the derivative of the edge region [57]. It should be noted that the absorption edge of pure Fe, FeO and Fe_2O_3 are found to be at 7112 eV, 7123.4 eV and 7126.8 eV respectively; whereas the absorption edge for the Fe doped LaGaO_3 samples ranges between 7127.1 eV to 7128.1 eV. The edge jump value is at higher side for Fe K-edge (as clear from XANES data) in Fe doped LaGaO_3 samples suggests that the fraction of Fe is present in oxidation state greater than +3 in the prepared samples, shown in the table of fig.(3.3.10)[41,58]. Here we are giving a representative calculation for oxygen stoichiometry in $\text{LaGa}_{0.7}\text{Fe}_{0.3}\text{O}_{3+\delta}$ sample using charge neutrality condition. Charge state of

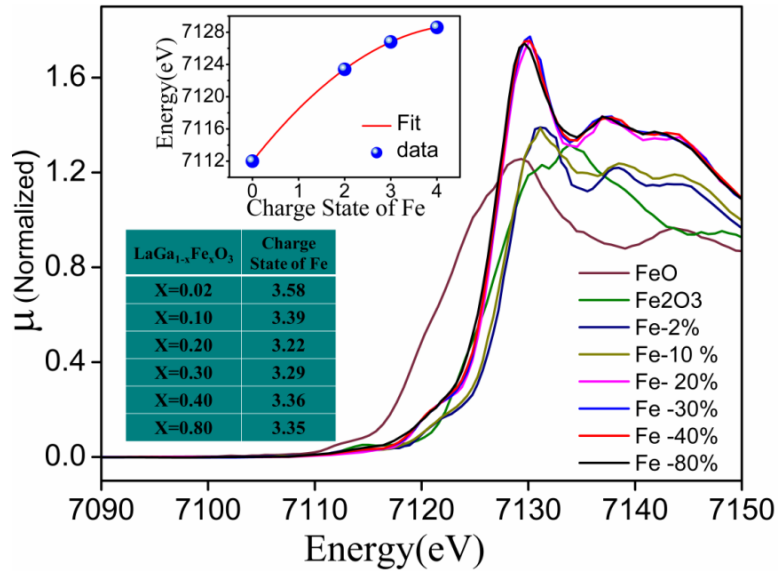


Fig.(3.3.10): Representative XANES spectra for the prepared Fe doped LaGaO₃ samples.

Fe in LaGa_{0.7}Fe_{0.3}O_{3+δ} is +3.29. By using charge neutrality condition...

$$La^{3+}Ga_{0.7}^{3+}Fe_{0.3}^{+3.29}O_{3+\delta}^{2-} = 0$$

$$OR, 3 \times 1 + 0.7 \times 3 + 3.29 \times 0.3 - 2(3 + \delta) = 0$$

$$OR, 3 + 2.1 + 0.987 - 6 = 2\delta$$

$$OR, \delta = \frac{0.087}{2} = 0.043$$

Also we have performed Iodometric titration (discussed in chapter 2) to verify the charge state of Fe in LaGa_{1-x}Fe_xO₃ samples. Here we are giving a representative calculation of 30% Fe doped LaGaO₃ sample. From titration experiment volume (V₁) used of sodium thiosulphate to get end point is 1.55ml, normality (N₁) of the thiosulphate is 0.1, weight of sample used for titration is 0.1007g and the molecular weight of 30% Fe doped LaGaO₃ sample is 252.4639g. So from the equation 2.9,

$$\delta = \frac{N_2 V_2 \times \text{Mol.Weight}}{2W_1} - 0.15$$

$$\text{OR, } \delta = \frac{0.1 \times 1.55 \times 10^{-3} \times 252.4639}{2 \times 0.1007} - 0.15$$

$$\text{OR, } \delta = 0.1942 - 0.15 = 0.044$$

Here it is clear that δ is positive, which suggest that Fe is in higher than +3 charge state.

Supposing that Fe is in +3 and +4 charge state, so by using charge neutrality condition

$$La^{+3}Ga_{0.7}^{+3}Fe_{0.3(1-x)}^{+3}Fe_{0.3x}^{+4}O_{3.044}^{-2} = 0$$

$$\text{OR, } 3 \times 1 + 0.7 \times 3 + 0.3(1-x) \times 3 + 0.3x \times 4 - 2 \times 3.044 = 0$$

$$\text{OR, } 3 + 2.1 + 0.9 - 0.9x + 1.2x - 6.088 = 0$$

$$\text{OR, } 0.3x = 0.088$$

$$\text{OR, } x = 0.29$$

So Fe^{4+} is 29% of whole Fe and remaining 71% is Fe^{3+} . From NANES data and titration data it is clear that these two are in complete agreement with each other and Fe is in mixed charge state of Fe^{+3} and Fe^{+4} .

After describing the results, the summarized view of the present thesis work and also the future scope has been given in next chapter.

CHAPTER 4

Summary, Conclusion and Future Scope

Summary:

- 1) The XRD results show that all the prepared samples are pure and are in single crystallographic and chemical phase.
- 2) The lattice parameters of Fe doped LaGaO₃ systematically changing with Fe doping and follow the Vegard's law.
- 3) DRS results show that the band gap changing systematically with Fe doping, it decreases systematically upto 40% of Fe doping and become almost constant with higher doping for direct as well as indirect band gap calculation.
- 4) By fitting the Vegard's equation bowing parameter is calculated for both direct and indirect band gap and is found around 3.43 eV for direct band gap and 3.59 eV for indirect band gap.
- 5) The dielectric measurements with and without fields are performed and in 30% Fe doped sample we could see a huge magneto-dielectric coupling which is extrinsic at low frequency $< 10^4$ Hz (due to magneto-resistance) and intrinsic at higher frequency $\geq 10^5$ Hz.

Conclusions and New findings in this thesis work: In conclusion we have produced

- 1) A high sensitive low field room temperature magneto-dielectric material which is first of its kind.
- 2) The optical band gap of LaGaO₃ can be tuned with Fe doping.

My learning and understanding through the project work:

- The solid state powdered samples are prepared by conventional solid state reaction method and their purity depends on the method of synthesis that how precisely synthesis is performed.
- Understanding of doping mechanism and role of impurity in samples.
- Structural characterization has been done using XRD. Effect of doping and the change in the lattice parameter has been studied by XRD analysis.
- Optical characterization has been done using DRS. Change in the band gap due to the difference in the ionic radii of Ga and Fe and also the generation of new intensity peaks at lower energy side is studied by DRS results analysis.
- Dielectric characterization has been done in absence and presence of magnetic field at room temperature. The change in the dielectric constant with Fe doping is due to the mixed charge states of Fe.

Future Scope: Present work deals with synthesis of solid samples and their characterization using XRD, DRS and dielectric and magneto-dielectric measurements at room temperature. There are some possible scopes to extend this work further in future as:

- Photoluminescence studies need to confirm the nature of the band gap in the prepared samples
- The temperature depended dielectric, magneto-dielectric and magnetization measurements.
- Temperature and magnetic field dependent XRD to understand the origin of magneto-dielectric coupling.

References:

- [1] T. Ishihara, J. Tabuchi, S. Ishikawa, J. Yan, M. Enoki, H. Matsumoto, *Solid State Ionics* **177** (2006) 1949–1953.
- [2] *Future Trends in Microelectronics: Frontiers and Innovations* - Serge Luryi, Jimmy Xu, Alexander Zaslavsky.
- [3] *Nanoscale Phase Separation and Colossal Magnetoresistance* - Elbio Dagotto.
- [4] S. Ishiwata, Y. Taguchi, H. Murakawa, Y. Onose, Y. Tokura, *Science* **319** (2008) 1643–1646.
- [5] T. Kimura, T. Goto, H. Shintani, K. Ishizaka, T. Arima, Y. Tokura, *Nature* **426** (2003) 55–58.
- [6] M. Bibes, A. Barthélémy, *Nat Mater* **7** (2008) 425–426.
- [7] G. Lawes, A.P. Ramirez, C.M. Varma, M.A. Subramanian, *Phys. Rev. Lett.* **91** (2003) 257208.
- [8] H.M. Rai, R. Late, S.K. Saxena, V. Mishra, R. Kumar, P.R. Sagdeo, Archana Sagdeo, *Mater. Res. Express* **2** (2015) 096105.
- [9] M. Glowacki, T. Runka, V. Domukhovski, R. Diduszko, M. Mirkowska, M. Berkowski, B. Dabrowski, *Journal of Alloys and Compounds* **509** (2011) 1756–1759.
- [10] R. Aleksiyko, M. Berkowski, P. Byszewski, R. Diduszko, E. Kowalska, in: 2001, pp. **50–54**.
- [11] M. Feng, J.B. Goodenough, K. Huang, C. Milliken, *Journal of Power Sources* **63** (1996) 47–51.
- [12] T. Ishihara, M. Honda, T. Shibayama, H. Minami, H. Nishiguchi, Y. Takita, *J. Electrochem. Soc.* **145** (1998) 3177–3183.
- [13] Y. Shimizu, Y. Takano, K. Ueda, *Thin Solid Films* **559** (2014) 23–26.
- [14] K. Ogisu, A. Ishikawa, Y. Shimodaira, T. Takata, H. Kobayashi, K. Domen, *J. Phys. Chem. C* **112** (2008) 11978–11984.
- [15] X. Liu, J. Lin, *J. Mater. Chem.* **18** (2007) 221–228.
- [16] H.L. Li, H.L.W. Chan, J.H. Hao, *J. Phys. D: Appl. Phys.* **42** (2009) 185103.
- [17] H.K. Yang, B.K. Moon, B.C. Choi, J.H. Jeong, J.H. Kim, K.H. Kim, *Solid State Sciences* **14** (2012) 236–240.

- [18] H.M. Rai, S.K. Saxena, R. Late, V. Mishra, P. Rajput, A. Sagdeo, R. Kumar, P.R. Sagdeo, *RSC Adv.* **6** (2016) 26621–26629.
- [19] A. Senyshyn, H. Ehrenberg, L. Vasylechko, J.D. Gale, U. Bismayer, *J. Phys.: Condens. Matter* **17** (2005) 6217.
- [20] J. Su, X. Lu, C. Zhang, J. Zhang, H. Sun, C. Ju, Z. Wang, K. Min, F. Huang, J. Zhu, *Physica B: Condensed Matter* **407** (2012) 485–488.
- [21] S. Acharya, J. Mondal, S. Ghosh, S.K. Roy, P.K. Chakrabarti, *Materials Letters* **64** (2010) 415–418.
- [22] K. Mori, T. Fukunaga, K. Shibata, K. Iwase, S. Harjo, A. Hoshikawa, K. Itoh, T. Kamiyama, T. Ishigaki, *Physica B: Condensed Matter* **352** (2004) 147–155.
- [23] M. Marezio, P.D. Dernier, *Materials Research Bulletin* **6** (1971) 23–29.
- [24] P.R. Sagdeo, S. Anwar, N.P. Lalla, *Powder Diffraction* **21** (2006) 40–44.
- [25] S.D. Singh, V. Nandanwar, H. Srivastava, A.K. Yadav, A. Bhakar, P.R. Sagdeo, A.K. Sinha, T. Ganguli, *Dalton Trans.* **44** (2015) 14793–14798.
- [26] L.W. Martin, *Dalton Trans.* **39** (2010) 10813–10826.
- [27] W. Eerenstein, N.D. Mathur, J.F. Scott, *Nature* **442** (2006) 759–765.
- [28] L. Vasylechko, A. Matkovski, A. Suchocki, D. Savytskii, I. Syvorotka, *Journal of Alloys and Compounds* **286** (1999) 213–218.
- [29] B.E. Warren, *X-Ray Diffraction*, Courier Corporation, 1969.
- [30] Kittel, *INTRODUCTION TO SOLID STATE PHYSICS*, 7TH ED, John Wiley & Sons, 2007.
- [31] C. Aydin, M.S. Abd El-sadek, K. Zheng, I.S. Yahia, F. Yakuphanoglu, *Optics & Laser Technology* **48** (2013) 447–452.
- [32] R.D. Shannon, *Acta Cryst. A* **32** (1976) 751–767.
- [33] P.R. Sagdeo, S. Anwar, N.P. Lalla, *Solid State Communications* **137** (2006) 158–161.
- [34] P.R. Sagdeo, S. Anwar, N.P. Lalla, *Phys. Rev. B* **74** (2006) 214118.
- [35] J.Q. Li, Y. Matsui, S.K. Park, Y. Tokura, *Phys. Rev. Lett.* **79** (1997) 297–300.
- [36] M. Vračar, A. Kuzmin, R. Merkle, J. Purans, E.A. Kotomin, J. Maier, O. Mathon, *Phys. Rev. B* **76** (2007) 174107.

- [37] V. Srihari, V. Sridharan, S. Chandra, V.S. Sastry, H.K. Sahu, C.S. Sundar, *Journal of Applied Physics* **109** (2011) 013510.
- [38] E.A. Davis, N.F. Mott, *Philosophical Magazine* **22** (1970) 0903–0922.
- [39] C. Chen, K.-C.Cheng, E. Chagarov, J. Kanicki, *Japanese Journal of Applied Physics* **50** (2011) 091102.
- [40] H. Han, J.W. Mayer, T.L. Alford, *Journal of Applied Physics* **100** (2006) 083715.
- [41] A. Sagdeo, K. Gautam, P.R. Sagdeo, M.N. Singh, S.M. Gupta, A.K. Nigam, R. Rawat, A.K. Sinha, H. Ghosh, T. Ganguli, A. Chakrabarti, *Applied Physics Letters* **105** (2014) 042906.
- [42] M.D. Scafetta, A.M. Cordi, J.M. Rondinelli, S.J. May, *Journal of Physics: Condensed Matter* **26** (2014) 505502.
- [43] G.G. Raju, *Dielectrics in Electric Fields*, CRC Press, 2003.
- [44] K. Świątek, M. Godlewski, *Applied Physics Letters* **56** (1990) 2192–2194.
- [45] X. Mao, H. Sun, W. Wang, X. Chen, Y. Lu, *Applied Physics Letters* **102** (2013) 072904.
- [46] C.-H. Yang, S.-H.Lee, T.Y. Koo, Y.H. Jeong, *Phys. Rev. B* **75** (2007) 140104.
- [47] R.S. Freitas, J.F. Mitchell, P. Schiffer, *Phys. Rev. B* **72** (2005) 144429.
- [48] Y. Kitagawa, Y. Hiraoka, T. Honda, T. Ishikura, H. Nakamura, T. Kimura, *Nat Mater* **9** (2010) 797–802.
- [49] X. Wu, X. Wang, Y. Liu, W. Cai, S. Peng, F. Huang, X. Lu, F. Yan, J. Zhu, *Applied Physics Letters* **95** (2009) 182903.
- [50] M. Sánchez-Andújar, S. Yáñez-Vilar, N. Biskup, S. Castro-García, J. Mira, J. Rivas, M.A. Señaris-Rodríguez, *Journal of Magnetism and Magnetic Materials* **321** (2009) 1739–1742.
- [51] G. Catalan, *Appl. Phys. Lett.* **88** (2006) 102902.
- [52] A. Shahee, R.J. Choudhary, R. Rawat, A.M. Awasthi, N.P. Lalla, *Solid State Communications* **177** (2014) 84–88.
- [53] K.D. Chandrasekhar, A.K. Das, A. Venimadhav, *J. Phys.: Condens. Matter* **24** (2012) 376003.
- [54] Z.X. Cheng, H. Shen, J.Y. Xu, P. Liu, S.J. Zhang, J.L. Wang, X.L. Wang, S.X. Dou, *Journal of Applied Physics* **111** (2012) 034103.

- [55] M.A. El Hiti, *Journal of Magnetism and Magnetic Materials* **192** (1999) 305–313.
- [56] W. Wang, L.-Q. Yan, J.-Z. Cong, Y.-L. Zhao, F. Wang, S.-P. Shen, T. Zou, D. Zhang, S.-G. Wang, X.-F. Han, Y. Sun, *Scientific Reports* **3** (2013) 2024.
- [57] A. Gaur, B.D. Shrivastava, H.L. Nigam, *Proceedings of the Indian National Science Academy* **79** (2013) 921–966.
- [58] I. Arcon, B. Mirtic, A. Kodre, *Journal of the American Ceramic Society* **81** (1998) 222–224.